PTEP

Prog. Theor. Exp. Phys. **2022** 093D03(37 pages)
DOI: 10.1093/ptep/ptac115

Kaon–baryon coupling schemes and kaon condensation in hyperon-mixed matter

Takumi Muto [1,*], Toshiki Maruyama[2], and Toshitaka Tatsumi[3]

[1] *Department of Physics, Chiba Institute of Technology, 2-1-1 Shibazono, Narashino, Chiba 275-0023, Japan*
[2] *Advanced Science Research Center, Japan Atomic Energy Agency, Ibaraki 319-1195, Japan*
[3] *Kitashirakawa Kamiikeda-Cho, 52-4, Kyoto 606-8287, Japan*
*E-mail: takumi.muto@it-chiba.ac.jp

Received July 1, 2022; Accepted August 16, 2022; Published August 26, 2022

The possible coexistence of kaon condensation and hyperons in highly dense matter [the $(Y + K)$ phase] is investigated on the basis of the relativistic mean-field theory combined with the effective chiral Lagrangian. Two coupling schemes for the s-wave kaon–baryon interaction are compared regarding the onset density of kaon condensation in hyperon-mixed matter and the equation of state for the developed $(Y + K)$ phase. One is the contact interaction scheme related to the nonlinear effective chiral Lagrangian. The other is the meson exchange scheme, where the interaction vertices between the kaon field and baryons are described by an exchange of mesons (σ, σ^* mesons for scalar coupling, and ω, ρ, ϕ mesons for vector coupling). It is shown that in the meson exchange scheme, the contribution from the nonlinear scalar self-interaction gives rise to a repulsive effect for the kaon effective energy, pushing up the onset density of kaon condensation as compared with the contact interaction scheme. In general, the difference in kaon–baryon dynamics between the contact interaction scheme and the meson exchange scheme relies on the specific forms of the nonlinear self-interacting meson terms. They generate many-baryon forces through the equations of motion for the meson mean fields. However, they should have a definite effect on the ground state properties of nuclear matter only around the saturation density. It is shown that the nonlinear self-interacting term is not relevant to repulsive energy leading to stiffening of the equation of state at high densities, and that it cannot be compensated with a large attractive energy due to the appearance of the $(Y + K)$ phase in the case of the contact interaction scheme. We also discuss what effects are necessary in the contact interaction scheme to make the equation of state with $(Y + K)$ phase stiff enough to be consistent with recent observations of massive neutron stars.

Subject Index D33

1. Introduction

Multi-strangeness systems in dense hadronic matter have been investigated extensively from nuclear and astrophysical points of view. As a possible form for neutron stars, Bose–Einstein condensation of anti-kaons (K^-) (kaon condensation) has been attracting much interest as a macroscopic form of strangeness degree of freedom [1–12], and its implications for astrophysical phenomena related to compact stars have been discussed: It has a large impact on the structure and thermal evolution of neutron stars through softening of the equation of state (EOS) [7,10] and enhancement of neutrino emissions [2,5,6].

It has been shown that the s-wave kaon condensation can be discussed model independently on the basis of current algebra and partial conservation of axial-vector current (PCAC) [2,3,5].

A series of works based on chiral symmetry have shown that kaon condensation arises at baryon number density $\rho_B = (3-4)\rho_0$, with ρ_0 being the normal nuclear density, for the value of the KN sigma term, $\Sigma_{KN} = (300-400)$ MeV, which simulates explicit chiral symmetry breaking [3,5,7,9,10]. In these approaches, the s-wave kaon–baryon (K–B) interaction is represented within the contact interaction (CI) scheme, where the structure of K–B and kaon–kaon (K–K) interaction vertices becomes nonlinear and is inherently determined from chiral symmetry.

As another hadron phase with multi-strangeness, it has been suggested that hyperons ($Y = \Lambda$, Σ^-, Ξ^-, …) are mixed (Y-mixing) in the ground state of neutron star matter by the use of the relativistic mean-field (RMF) theories [13–21], many-body approaches based on reaction matrix theory, variational methods, and so forth [22–28]. The mixing of hyperons also leads to softening of the EOS [13,18–20,22–26,28] and provides another candidate for rapid cooling of neutron stars [29,30]. The onset density of hyperons, $\rho_{\rm B}^c(Y)$, has been estimated to be $\rho_B = (2-4)\rho_0$. Thus it may be plausible that kaon condensates and hyperons may coexist in dense neutron star matter.

One of the authors (T. Muto) has considered the possible coexistence of a kaon-condensed phase and hyperon-mixed matter [abbreviated to the $(Y + K)$ phase in this paper] in neutron stars using the effective chiral Lagrangian for the s-wave K–B interaction and a phenomenological potential model for baryon–baryon (B–B) interactions [31]. One of the serious problems resulting from the existence of the $(Y + K)$ phase is that both kaon condensates and Y-mixing in dense matter lead to significant softening of the EOS, which is not compatible with recent observations of massive neutron stars with $(1.928 \pm 0.017)\, M_\odot$ for PSR J1614-2230 and $(2.01 \pm 0.04)\, M_\odot$ for PSR J0348+0432, where $M_\odot$ is the solar mass [32–34]. Pulsars definitely exceeding $2\, M_\odot$ have been detected, such as $(2.08 \pm 0.07)\, M_\odot$ for the 2.8 ms radio pulsar PSR J0740+6620 [35,36] and $(2.13 \pm 0.04)\, M_\odot$ for PSR J1810+1744 [37]. The coexistence of kaon condensation and hyperons in dense matter has also been discussed by several authors in terms of RMF theories [14–17,38,39], effective chiral models [40,41], and quark–meson coupling models [42,43]. Most of the models including the $(Y + K)$ phase predict maximum neutron star masses of less than $1.85\, M_\odot$ except for recent works with density-dependent meson–baryon coupling strengths in the RMF [44–46].

Recent progress in observational facilities and satellites has provided new information on the structure of compact stars. The detection of gravitational waves from neutron star mergers (GW170817) by the LIGO-Virgo collaboration [47] has shed light on constraining the EOS of dense matter by setting limits on the tidal deformabilities of compact stars [48,49]. The precise measurement of masses and radii of neutron stars has become possible from the X-ray observations of Neutron star Interior Composition ExploreR (NICER) [50,51]. The mass and radius for the above-mentioned pulsar PSR J0740+6620 has been detected as $R = (12.35 \pm 0.75)$ km for $M = 2.08\, M_\odot$ [52] and $R = (12.39^{+1.30}_{-0.98})$ km for $M = (2.072^{+0.067}_{-0.066})\, M_\odot$ [53]. The EOS including the $(Y + K)$ phase should be in conformity with stringent constraints deduced from these observations.

Studies of kaon condensation in neutron stars have triggered research on deeply bound kaonic states which may be formed in terrestrial experiments [54–61], and associated kaon dynamics in the nuclear medium has been extensively studied theoretically and experimentally [60–62]. Recently, the formation of basic kaonic clusters, K^-pp, has been reported in the E27 and E15 experiments at J-PARC [63–66].

In order to find out the connection between deeply bound kaonic states in nuclei and kaon condensation in dense matter, we have studied multi-anti-kaonic bound states in nuclei based on the RMF theory coupled to the effective chiral Lagrangian [57]. In this framework, we have adopted the meson exchange (ME) scheme for the s-wave K–B interaction, where the CI vertices between the nonlinear kaon field and baryons in the original effective chiral Lagrangian are replaced by an exchange of mesons (scalar mesons σ, σ^* and vector mesons ω, ρ, ϕ). (We called this interaction model the "chiral model" in Ref. [57].) Thus, many-body effects on the K–B interaction coming from the meson exchange in a nuclear medium can be taken into account in the ME scheme. In a series of works we have considered not only possible bound states of kaons and hyperons in nuclei (kaon-condensed hypernuclei) but also the $(Y + K)$ phase in neutron stars within the same interaction model based on the ME scheme and discussed the interplay of kaons and hyperons in multi-strangeness systems in a unified way for both nuclei and neutron stars [67]. It is to be noted that the "chiral model" based on the ME scheme reduces essentially to the meson exchange model in the limit of linear approximation for nonlinear kaon fields [57]. The meson exchange model has been utilized by several authors to describe kaon condensation [14–17,38,40] and multi-anti-kaonic nuclei [58] in the context of the RMF theories.

Toward a description of the $(Y + K)$ phase consistent with the recent observations of massive neutron stars or gravitational waves from neutron star merger, we should start by removing the uncertainties stemming from the s-wave K–B interaction, since this is a driving force for kaon condensation and may crucially affect the onset density and the EOS of the $(Y + K)$ phase, depending on the choice of coupling schemes for the s-wave K–B interaction.

In this paper we first discuss in detail the validity of the CI and ME coupling schemes for the K–B interaction vertices based on the effective chiral Lagrangian coupled to the RMF model. We take into account the nonlinear self-interacting (NLSI) potential term of the σ mesons, U_σ, which is usually introduced phenomenologically, in addition to the two-body B–B interactions which are mediated by scalar and vector mesons in the RMF framework. [Throughout this paper, we call this two-body B–B interaction part of the model the "minimal RMF" (MRMF).] The results on the onset density and characteristic features of the $(Y + K)$ phase in these two schemes based on the (MRMF+NLSI) model are compared. It is shown that the effect of the NLSI term is propagated to the kaon self-energy in the ME scheme as a derivative term, $dU_\sigma/d\sigma$, through the equation of motion for the σ meson. (Similar results have been pointed out in Refs. [15,16].) Such a model-dependent term is added as an extra repulsive contribution to the lowest kaon energy in the ME scheme beyond the scope of chiral symmetry. As a result, kaon condensation from hyperon-mixed matter does not occur in the case of the ME scheme unless Σ_{KN} is taken to be very large. On the other hand, in the CI scheme, the K–B and K–K interactions are controlled model independently within chiral symmetry. It will be shown that the onset density for kaon condensation realized from hyperon-mixed matter and the EOS with the $(Y + K)$ phase are obtained with moderate values of Σ_{KN} [$= (300-400)$ MeV].

Second we consider the role of the NLSI term, which generates many-baryon forces through the equations of motion for the meson mean fields, as a possible origin of repulsive forces at high densities in view of a solution to the "hyperon puzzle." It will be shown that the NLSI term poses quite different aspects for the saturation mechanisms of symmetric nuclear matter (SNM) from those in the conventional variational methods with phenomenological three-baryon forces. Further, the NLSI term becomes only a minor contribution to the repulsive energy at high densities, not being able to make the EOS stiff enough to be consistent with

recent observations of massive neutron stars. We address that the universal three-baryon repulsive forces (UTBR), as introduced phenomenologically in place of the NLSI meson terms in our recent work [68], can make the EOS with the $(Y + K)$ phase stiff enough to reconcile theories with observations. It is also pointed out that the kaon self-energy in hyperon-mixed matter with such UTBR is formally equivalent between the CI and ME schemes.

The paper is organized as follows. Section 2 gives an overview of the $(Y + K)$ phase in the context of chiral symmetry. The *s*-wave *K*–*B* interaction in the CI scheme and the baryon–baryon (*B*–*B*) interaction in the (MRMF+NLSI) model are described in Sects. 3 and 4, respectively. Section 5 gives the energy expression for the $(Y + K)$ phase in the CI scheme. In Sect. 6, the formulation in the ME scheme is explained, and the CI and ME schemes are compared. The numerical results on the onset density of kaon condensation are presented in Sect. 7, where the effects of the NLSI term as many-baryon forces are discussed. In Sect. 8, the roles of the NLSI term on saturation mechanisms in SNM and on the EOS of the $(Y + K)$ phase in the CI scheme are described. In Sect. 9, properties of the $(Y + K)$ phase, for instance the density dependence of particle fractions and hyperon potentials in the CI scheme, are addressed with the (MRMF+NLSI) model as common features in the presence of kaon condensates. The self-suppression effect of the *s*-wave *K*-*B* attraction unique to the case of kaon condensation in the RMF framework is also discussed. In Sect. 10, our alternative model with the UTBR in the RMF in place of the NLSI term is described, and circumventing the problem caused by the NLSI term, which is connected with avoiding the extra many-body effect in the ME scheme, is discussed. A summary and concluding remarks are provided in Sect. 11. In Appendix A, the allowable value of Σ_{Kn} is evaluated. In Appendix B, the K^- optical potential depths are derived in both the CI and ME schemes and related to the *s*-wave scalar *K*–*N* interaction, the *KN* sigma terms.

2. Overview of the $(Y + K)$ phase

To describe the $(Y + K)$ phase, we use the $\mathrm{SU(3)_L \times SU(3)_R}$ chiral effective Lagrangian, where the nonlinear representation of the kaon field is given as $U = \exp[2i(K^+ T_{4+i5} + K^- T_{4-i5})/f]$, with $T_{4\pm i5}$ ($\equiv T_4 \pm iT_5$) being the flavor SU(3) generators and f the meson decay constant. The numerical value of f is set to that of the pion decay constant ($f_\pi = 93$ MeV) instead of the kaon decay constant ($f_K = 113$ MeV) following our previous papers [3–6,10], which corresponds to taking the lowest-order value in chiral perturbation theory under the SU(3) flavor symmetry. On the basis of chiral symmetry, the *s*-wave kaon-condensed state, $|K\rangle$, is represented by chiral rotation from the normal state, and the classical kaon field stands for an order parameter for kaon condensation [2,3,12]. Here it is taken to be spatially uniform with momentum $\mathbf{k} = 0$:

$$K^\pm = \frac{f}{\sqrt{2}}\theta \exp(\pm i\mu_K t), \tag{1}$$

where θ is the chiral angle, and μ_K is the K^- chemical potential. U is expressed explicitly in terms of Eq. (1) as

$$U = 1 + iA\sin\theta + A^2(\cos\theta - 1), \tag{2}$$

with the matrix A being defined by

$$A = \begin{pmatrix} 0 & 0 & K^+/|K| \\ 0 & 0 & 0 \\ K^-/|K| & 0 & 0 \end{pmatrix}, \tag{3}$$

where $|K| \equiv (K^+K^-)^{1/2} = f\theta/\sqrt{2}$ [1].

The $(Y + K)$ phase consists of kaon condensates, degenerate baryons, and leptons in beta equilibrium. We take into account only protons (p), neutrons (n), Λ, Σ^-, Ξ^- for octet baryons, since degenerate leptons assist mixing of neutral or negatively charged hyperons through beta equilibrium conditions. For leptons, muons may appear at a density slightly higher than that of the electrons under consideration. However, the quantitative effects of muons on the properties of matter are expected to be small, so that we take into account only electrons (e^-) for simplicity. We impose the charge neutrality condition and baryon number conservation, and construct the effective energy density $\mathcal{E}_{\rm eff}$ by introducing the charge chemical potential μ and the baryon number chemical potential ν as Lagrange multipliers. The resulting effective energy density is then written in the form

$$\mathcal{E}_{\rm eff} = \mathcal{E} + \mu(\rho_p - \rho_{\Sigma^-} - \rho_{\Xi^-} - \rho_{K^-} - \rho_e) + \nu(\rho_p + \rho_\Lambda + \rho_n + \rho_{\Sigma^-} + \rho_{\Xi^-}), \tag{4}$$

where $\mathcal{E}$ is the total energy density of the kaon-condensed phase, and ρ_i ($i = p$, n, Λ, Σ^-, Ξ^-, K^-, e^-) is the number density of the particle i.

The classical kaon field equation is given from $\partial\mathcal{E}_{\rm eff}/\partial\theta = 0$. From the extremum conditions for $\mathcal{E}_{\rm eff}$with respect to variation of ρ_i, one obtains the relations

$$\mu_K = \mu_e = \mu, \tag{5a}$$

$$\mu_p = -\mu - \nu, \tag{5b}$$

$$\mu_{\Sigma^-} = \mu_{\Xi^-} = \mu - \nu, \tag{5c}$$

$$\mu_\Lambda = \mu_n = -\nu, \tag{5d}$$

where μ_i ($i = p$, Λ, n, Σ^-, Ξ^-, K^-, e^-) are the chemical potentials, which are given by $\mu_i = \partial\mathcal{E}/\partial\rho_i$. Obviously, Eqs. (5a)–(5d) imply that the system is in chemical equilibrium for the weak interaction processes $n \rightleftharpoons p + K^-$, $n \rightleftharpoons p + e^-(+\bar{\nu}_e)$, $n + e^- \rightleftharpoons \Sigma^-(+\nu_e)$, $\Lambda + e^- \rightleftharpoons \Xi^-(+\nu_e)$, and $n \rightleftharpoons \Lambda(+\nu_e\bar{\nu}_e)$.

3. *S*-wave *K*–*B* interaction in the contact interaction scheme

The effective chiral Lagrangian for kaons and baryons in the CI scheme [1] is given by

$$\begin{aligned}\mathcal{L}_{K,B} = {} & \frac{1}{4}f^2\,{\rm Tr}\partial^\mu U^\dagger\partial_\mu U + \frac{1}{2}f^2\Lambda_{\chi{\rm SB}}({\rm Tr}M(U-1) + {\rm h.c.}) + {\rm Tr}\overline{\Psi}(i\gamma^\mu\partial_\mu - M_B)\Psi \\ & + {\rm Tr}\overline{\Psi}i\gamma^\mu[V_\mu, \Psi] + D{\rm Tr}\overline{\Psi}\gamma^\mu\gamma^5\{A_\mu, \Psi\} + F{\rm Tr}\overline{\Psi}\gamma^\mu\gamma^5[A_\mu, \Psi] \\ & + a_1{\rm Tr}\overline{\Psi}(\xi M^\dagger\xi + {\rm h.c.})\Psi + a_2{\rm Tr}\overline{\Psi}\Psi(\xi M^\dagger\xi + {\rm h.c.}) + a_3({\rm Tr}MU + {\rm h.c.}){\rm Tr}\overline{\Psi}\Psi,\end{aligned} \tag{6}$$

where the first and second terms on the right-hand side are the kinetic and mass terms of kaons U in the nonlinear representation, respectively, $\Lambda_{\chi{\rm SB}}$ is the chiral symmetry breaking scale ($\sim$1 GeV), and M the quark mass matrix, $M \equiv {\rm diag}(m_u, m_d, m_s)$ with the quark masses m_i [1]. The free kaon mass is identified with $m_K = [\Lambda_{\chi{\rm SB}}(m_u + m_s)]^{1/2}$ and is set to be the empirical value (= 494 MeV). The third term in Eq. (6) denotes the kinetic and mass terms for baryons, where M_B is the baryon mass generated by spontaneous breaking of chiral symmetry. The fourth term in Eq. (6) gives the s-wave K–B vector interaction corresponding to the Tomozawa–Weinberg term, with V_μ being the mesonic vector current defined by $V_\mu \equiv 1/2(\xi^\dagger\partial_\mu\xi + \xi\partial_\mu\xi^\dagger)$ with $\xi \equiv U^{1/2}$. The fifth and sixth terms are the K–B axial-vector interaction with the mesonic

axial-vector current defined by $A_\mu \equiv i/2(\xi^\dagger \partial_\mu \xi - \xi \partial_\mu \xi^\dagger)$. Throughout this paper we simply omit these axial-vector coupling terms and retain only the s-wave K–B vector interaction in order to figure out the consequences from s-wave kaon condensation. The last three terms in Eq. (6) give the s-wave K–B scalar interaction, which explicitly breaks chiral symmetry.

Using Eq. (1), the Lagrangian density Eq. (6) is separated into a baryon part $\mathcal{L}_B$ and kaon part $\mathcal{L}_K$ in the mean-field approximation. For $\mathcal{L}_B$ one obtains

$$\mathcal{L}_B = \sum_{b=p,n,\Lambda,\Sigma^-,\Xi^-} \overline{\psi_b}(i\gamma^\mu \partial_\mu - M_b^*)\psi_b, \tag{7}$$

where the s-wave K–B scalar interaction is absorbed into the effective baryon mass M_b^*:

$$M_b^* = M_b - \Sigma_{Kb}(1 - \cos\theta), \tag{8}$$

with M_b ($b = p$, n, Λ, Σ^-, Ξ^-) being the baryon mass defined by

$$\begin{aligned}
M_p &= M_B - 2(a_1 m_u + a_2 m_s) - 2a_3(m_u + m_d + m_s),\\
M_n &= M_B - 2(a_1 m_d + a_2 m_s) - 2a_3(m_u + m_d + m_s),\\
M_\Lambda &= M_B - 1/3 \cdot (a_1 + a_2)(m_u + m_d + 4m_s) - 2a_3(m_u + m_d + m_s),\\
M_{\Sigma^-} &= M_B - 2(a_1 m_d + a_2 m_u) - 2a_3(m_u + m_d + m_s),\\
M_{\Xi^-} &= M_B - 2(a_1 m_s + a_2 m_u) - 2a_3(m_u + m_d + m_s),
\end{aligned} \tag{9}$$

and Σ_{Kb} being the "K-baryon sigma term" which simulates the K–B attractive interaction in the scalar channel [4,31]:

$$\Sigma_{Kp} = \Sigma_{K\Xi^-} = -(a_1 + a_2 + 2a_3)(m_u + m_s), \tag{10a}$$

$$\Sigma_{Kn} = \Sigma_{K\Sigma^-} = -(a_2 + 2a_3)(m_u + m_s), \tag{10b}$$

$$\Sigma_{K\Lambda} = -\left(\frac{5}{6}a_1 + \frac{5}{6}a_2 + 2a_3\right)(m_u + m_s) \tag{10c}$$

(see Appendix A1). In the following, M_b ($b = p$, n, Λ, Σ^-, Ξ^-) [Eq. (9)] are identified with the empirical baryon masses, i.e. $M_p = 938.27$ MeV, $M_n = 939.57$ MeV, $M_\Lambda = 1115.68$ MeV, $M_{\Sigma^-} = 1197.45$ MeV, and $M_{\Xi^-} = 1321.71$ MeV.

Following Ref. [1], the quark masses m_i are chosen to be $m_u = 6$ MeV, $m_d = 12$ MeV, and $m_s = 240$ MeV. Together with these values, the parameters a_1 and a_2 are fixed to be $a_1 = -0.28$, $a_2 = 0.56$ to reproduce the empirical octet baryon mass splittings [1]. The remaining parameter a_3 is fixed to give the KN sigma term, Σ_{KN}. Throughout this paper we consider two cases as allowable values of Σ_{Kn}: $\Sigma_{Kn} = 300$ MeV and 400 MeV, for which $a_3 = -0.89$ and -1.1, respectively. In these cases one also obtains, from Eqs. (10a)–(10c), $\Sigma_{K\Sigma^-} = 300$ MeV, $\Sigma_{Kp} = \Sigma_{K\Xi^-} = 369$ MeV, and $\Sigma_{K\Lambda} = 380$ MeV for $a_3 = -0.89$, and $\Sigma_{K\Sigma^-} = 400$ MeV, $\Sigma_{Kp} = \Sigma_{K\Xi^-} = 469$ MeV, and $\Sigma_{K\Lambda} = 480$ MeV for $a_3 = -1.1$. According to the lattice QCD result, the current quark masses have been fixed to be rather smaller values, $(m_u, m_d, m_s) = (2.2, 4.7, 95)$ MeV [70], than adopted in this paper. However, it can be shown that the Σ_{KN} is little altered by the use of different quark masses as far as $(m_u + m_s)/\hat{m}$ ($\sim$14) is almost the same in both set of quark masses [68].

For $\mathcal{L}_K$ one obtains [69]

$$\mathcal{L}_K = \frac{1}{2}\left\{1+\left(\frac{\sin\theta}{\theta}\right)^2\right\}\partial^\mu K^+\partial_\mu K^- + \frac{1-\left(\frac{\sin\theta}{\theta}\right)^2}{2f^2\theta^2}\left\{(K^+\partial_\mu K^-)^2+(K^-\partial_\mu K^+)^2\right\}$$
$$- m_K^2\left(\frac{\sin(\theta/2)}{\theta/2}\right)^2 K^+K^- + iX_0\left(\frac{\sin(\theta/2)}{\theta/2}\right)^2\left(K^+\partial_0 K^- - \partial_0 K^+K^-\right)$$
$$= \frac{1}{2}(f\mu_K\sin\theta)^2 - f^2m_K^2(1-\cos\theta) + 2\mu_K X_0 f^2(1-\cos\theta). \tag{11}$$

The last term on the right-hand side of Eq. (11) stands for the *s*-wave *K*–*B* vector interaction, with X_0 being given by

$$X_0 \equiv \frac{1}{2f^2}\sum_{b=p,n,\Lambda,\Sigma^-,\Xi^-} Q_V^b\rho_b = \frac{1}{2f^2}\left(\rho_p+\frac{1}{2}\rho_n-\frac{1}{2}\rho_{\Sigma^-}-\rho_{\Xi^-}\right), \tag{12}$$

where $Q_V^b \equiv \frac{1}{2}\left(I_3^{(b)}+\frac{3}{2}Y^{(b)}\right)$ is the V-spin charge with $I_3^{(b)}$ and $Y^{(b)}$ being the third component of the isospin and hypercharge for baryon species b, respectively. The form of Eq. (12) for X_0 is specified model independently within chiral symmetry. From Eqs. (11) and (12), one can see that the *s*-wave *K*–*B* vector interaction works attractively for protons and neutrons, while repulsively for Σ^- and Ξ^- hyperons, as far as $\mu_K > 0$.

In Ref. [71] we improved our model for the *s*-wave *K*–*B* interaction by introducing the range terms and a pole contribution from $\Lambda(1405)$ (denoted as Λ^*) so as to reproduce the on-shell *s*-wave *KN* scattering lengths [72]. It has been shown that the range terms work repulsively, and that the onset density of kaon condensation realized from hyperon-mixed matter is slightly pushed up to a higher density as compared with the case without the range terms. Nevertheless, the repulsive effect from the range terms ($\propto \mu_K^2$) on the EOS of the ($Y+K$) phase is tiny over the relevant densities as far as $\mu_K \lesssim O(m_\pi)$. The contribution from the Λ^* pole to the energy is also negligible over the baryon density $\rho_B \gtrsim \rho_0$, since the kaon energy in matter lies well below the pole position of $M_{\Lambda^*} - M_N$. Therefore, these effects of the range terms and the pole contribution from Λ^* are omitted in this paper.

4. *B*–*B* interaction in the RMF

4.1 *Lagrangian density for baryons and mesons*

In the RMF framework, the *B*–*B* interaction is mediated by scalar (σ, σ^*) and vector (ω, ρ, ϕ) mesons. The scalar meson σ^* ($\sim \bar{s}s$) and the vector meson ϕ ($\sim \bar{s}\gamma^\mu s$), both of which carry the strangeness and couple only to hyperons (Y), are introduced according to the extension of baryons to include hyperons. The quark structure of the ϕ meson comes from the assumption of an ideal mixing between ω and ϕ mesons. The scalar meson–baryon couplings lead to modification of the effective baryon masses in Eq. (8) to

$$\widetilde{M}_b^* = M_b - g_{\sigma b}\sigma - g_{\sigma^* b}\sigma^* - \Sigma_{Kb}(1-\cos\theta), \tag{13}$$

with $g_{\sigma b}$ ($b = p, n, \Lambda, \Sigma^-, \Xi^-$) and $g_{\sigma^* Y}$ ($Y = \Lambda, \Sigma^-, \Xi^-$) being the scalar meson–baryon coupling constants. The vector meson–baryon couplings are introduced by the covariant derivatives at the baryon kinetic terms as $\partial_\mu \to D_\mu^{(b)} \equiv \partial_\mu + ig_{\omega b}\omega_\mu + i\widetilde{g}_{\rho b}\vec{I}^{(b)}\cdot\vec{R}_\mu + ig_{\phi b}\phi_\mu$, where ω^μ, $\vec{R}^\mu$, and ϕ^μ denote the vector meson fields for ω, ρ, and ϕ mesons, respectively. The arrow attached to the ρ-meson field $\vec{R}_\mu$ refers to an isovector with the isospin operator $\vec{I}^{(b)}$ for baryon b. The $g_{\omega b}$, $\widetilde{g}_{\rho b}$, and $g_{\phi b}$ in the covariant derivative are the vector meson–baryon cou-

pling constants. It is to be noted that the ρ-meson–baryon coupling constant, $g_{\rho b}$, is factorized as $g_{\rho b} \equiv \widetilde{g}_{\rho b} \cdot |I_3^{(b)}|$ with the third component of the isospin for the baryon b. The ρ-meson–baryon coupling constants utilized in the other RMF models mostly correspond to $\widetilde{g}_{\rho b}$ in our model.

The baryon part of the Lagrangian density $\mathcal{L}_B$ is then modified from Eq. (7) to

$$\mathcal{L}_B = \sum_{b=p,n,\Lambda,\Sigma^-,\Xi^-} \overline{\psi_b}(i\gamma^\mu D_\mu^{(b)} - \widetilde{M}_b^*)\psi_b. \tag{14}$$

In addition, the meson part of the Lagrangian density, $\mathcal{L}_M$, including the σ self-interaction is introduced:

$$\begin{aligned}\mathcal{L}_M = {} & \frac{1}{2}\left(\partial^\mu\sigma\partial_\mu\sigma - m_\sigma^2\sigma^2\right) - U_\sigma(\sigma) + \frac{1}{2}\left(\partial^\mu\sigma^*\partial_\mu\sigma^* - m_{\sigma^*}^2\sigma^{*2}\right) \\ & - \frac{1}{4}\omega^{\mu\nu}\omega_{\mu\nu} + \frac{1}{2}m_\omega^2\omega^\mu\omega_\mu - \frac{1}{4}\vec{R}^{\mu\nu}\cdot\vec{R}_{\mu\nu} + \frac{1}{2}m_\rho^2\vec{R}^\mu\cdot\vec{R}_\mu - \frac{1}{4}\phi^{\mu\nu}\phi_{\mu\nu} + \frac{1}{2}m_\phi^2\phi^\mu\phi_\mu. \end{aligned} \tag{15}$$

The second term on the right-hand side of Eq. (15) is the scalar self-interaction potential given by $U_\sigma(\sigma) = bM_N(g_{\sigma N}\sigma)^3/3 + c(g_{\sigma N}\sigma)^4/4$, with $b = 0.008659$ and $c = -0.002421$ [13,57]. $U_\sigma(\sigma)$ is introduced to set the incompressibility at the nuclear saturation density to be 240 MeV, which is consistent with an empirical value; $U_\sigma(\sigma)$ is solely considered here as the NLSI term. The kinetic terms of the vector mesons are given in terms of $\omega^{\mu\nu} \equiv \partial^\mu\omega^\nu - \partial^\nu\omega^\mu$, $\vec{R}^{\mu\nu} \equiv \partial^\mu\vec{R}^\nu - \partial^\nu\vec{R}^\mu$, and $\phi^{\mu\nu} \equiv \partial^\mu\phi^\nu - \partial^\nu\phi^\mu$. Throughout this paper, only the time components of the vector meson mean fields and the third component of the isovector ρ mean field are considered to describe the ground state of the system. We simply denote these components as ω_0, R_0, and ϕ_0. Then the ρ–B coupling term in the covariant derivative is rewritten as $i\widetilde{g}_{\rho b}I_3^{(b)}R_0 = ig_{\rho b}\hat{I}_3^{(b)}R_0$ with $g_{\rho b}$ $(= \widetilde{g}_{\rho b} \cdot |I_3^{(b)}|)$ and $\hat{I}_3^{(b)} \equiv I_3^{(b)}/|I_3^{(b)}|$, where $\hat{I}_3^{(b)}$ is assigned as $\hat{I}_3^{(p)}$=+1, $\hat{I}_3^{(n)} = \hat{I}_3^{(\Sigma^-)} = \hat{I}_3^{(\Xi^-)} = -1$.

In the CI scheme there is no direct kaon–meson (m) coupling ($m = \sigma, \sigma^*, \omega, \rho, \phi$) [see Eqs. (11) and (15)].

4.2 *Choice of meson–baryon coupling constants*

The values of $g_{\sigma N}$, $g_{\omega N}$, and $g_{\rho N}$, which are related to the N–N interaction, are determined so as to reproduce not only the properties of normal nuclear matter with saturation density $\rho_0 = 0.153\,\mathrm{fm}^{-3}$, the binding energy (= 16.3 MeV), and the symmetry energy (= 32.8 MeV), but also the proton-mixing ratio and density distributions of proton and neutron for normal nuclei [57]. One obtains $g_{\sigma N} = 6.39$, $g_{\omega N} = 8.72$, and $g_{\rho N} = 4.27$. The σ^*–N and ϕ–N couplings are not taken into account since they should be suppressed due to the OZI rule.

The vector meson couplings for the hyperon Y are obtained from the relations in the SU(6) symmetry [73]:

$$g_{\omega\Lambda} = g_{\omega\Sigma^-} = 2g_{\omega\Xi^-} = \frac{2}{3}g_{\omega N}, \tag{16a}$$

$$g_{\rho\Lambda} = 0,\ g_{\rho\Sigma^-} = 2g_{\rho\Xi^-} = 2g_{\rho N}, \tag{16b}$$

$$g_{\phi\Lambda} = g_{\phi\Sigma^-} = \frac{1}{2}g_{\phi\Xi^-} = -\frac{\sqrt{2}}{3}g_{\omega N}. \tag{16c}$$

The scalar (σ, σ^*) meson–hyperon couplings are determined from phenomenological analyses of recent hypernuclear experiments as far as possible. The scalar σ meson coupling for the hyperon Y, $g_{\sigma Y}$, is related to the potential depth of the hyperon Y ($Y = \Lambda$, Σ^-, Ξ^-) at $\rho_B = \rho_0$

in SNM, V_Y^N, which is written in the RMF as

$$V_Y^N = -g_{\sigma Y}\langle\sigma\rangle_0 + g_{\omega Y}\langle\omega_0\rangle_0, \tag{17}$$

with $\langle\sigma\rangle_0$ and $\langle\omega_0\rangle_0$ being the meson mean fields at $\rho_B = \rho_0$ in SNM. For $Y = \Lambda$, the single-Λ orbital energies in ordinary hypernuclei are fitted well with the Λ-nucleus single-particle potential with depth ~ -27 MeV [74]. Based on this result, V_Λ^N is set to be -27 MeV. One then obtains $g_{\sigma\Lambda} = 3.84$ from Eq. (17).

The depth of the Σ^- potential $V_{\Sigma^-}^N$ has been shown to be repulsive, according to recent theoretical calculations [75,76] and phenomenological analyses of (K^-, $\pi^\pm$) reactions at BNL [77,78], (π^-, K^+) reactions at KEK [79–81], and the Σ^- atom data [82]. Following Ref. [78], $V_{\Sigma^-}^N$ is set to be 23.5 MeV as a typical value, from which one obtains $g_{\sigma\Sigma^-} = 2.28$ from Eq. (17).

The depth of the Ξ^- potential in nuclear matter is set to be attractive, $V_{\Xi^-}^N = -14$ MeV, with reference to the experimental results deduced from (K^-, K^+) reactions, $(-14) - (-20)$ MeV [83,84]. One then obtains $g_{\sigma\Xi^-} = 1.94$ from Eq. (17).

The σ^* meson couplings for the hyperon Y, $g_{\sigma^* Y}$, are relevant to the Y–Y interaction as well as the binding energy of hypernuclei. From recent detection of double-Λ hypernuclei in the KEK-E176-E373 experiments, separation energies for two Λs, $B_{\Lambda\Lambda}$, have been obtained for several double-Λ hypernuclei [61]. For the "Hida event," the experimental value of the separation energy for the ground state of ${}^{11}_{\Lambda\Lambda}$Be has been estimated to be 20.83 ± 1.27 MeV [61,85]. We determined $g_{\sigma^*\Lambda}$ so as to reproduce the empirical values of $B_{\Lambda\Lambda}({}^{11}_{\Lambda\Lambda}\mathrm{Be})$ using the present B–B interaction model in the RMF extended to finite nuclei [57,67]. One finds $g_{\sigma^*\Lambda} = 7.2$, for which $B^{\rm th}_{\Lambda\Lambda}({}^{11}_{\Lambda\Lambda}\mathrm{Be}) \equiv B^{\rm th}({}^{11}_{\Lambda\Lambda}\mathrm{Be}) - B^{\rm exp}({}^{9}\mathrm{Be}) = 20.7$ MeV with $B^{\rm exp}({}^{9}\mathrm{Be}) = 58.16$ MeV [86]. [Throughout this paper, the superscript "exp" ("th") denotes an experimental value (a theoretical value obtained in our B–B interaction model).] In this case, the Λ-separation energy for ${}^{10}_{\Lambda}$Be is estimated to be $B^{\rm th}_{\Lambda}({}^{10}_{\Lambda}\mathrm{Be}) \equiv B^{\rm th}({}^{10}_{\Lambda}\mathrm{Be}) - B^{\rm exp}({}^{9}\mathrm{Be}) = 9.95$ MeV, whereas the experimental value for the ground-state peak (mixture of 1^- and 2^- states) at J-Lab is reported as 8.55 MeV [87]. It is to be noted that our B–B interaction model applied to finite nuclei assumes the local density approximation and spherical symmetry for the profiles of baryon density distributions, whereas the ${}^{11}_{\Lambda\Lambda}$Be nucleus has a clustering structure [85]. Furthermore a quantitatively accurate estimation in our model may not be expected for a few-body system such as ${}^{6}_{\Lambda\Lambda}$He (the "Nagara event"), although a precise extraction of the $\Lambda\Lambda$ binding energy $B_{\Lambda\Lambda}({}^{6}_{\Lambda\Lambda}\mathrm{He})$ and the bond energy $\Delta B_{\Lambda\Lambda}({}^{6}_{\Lambda\Lambda}\mathrm{He}) \equiv B_{\Lambda\Lambda}({}^{6}_{\Lambda\Lambda}\mathrm{He}) - 2B_\Lambda({}^{5}_{\Lambda}\mathrm{He})$ has been done experimentally [88,89].

For the σ^*–Ξ^- coupling, the bound on the Ξ^- hypernucleus was detected through the "Kiso" event, $\Xi^- + {}^{14}\mathrm{N} \to {}^{15}_{\Xi}\mathrm{C} \to {}^{10}_{\Lambda}\mathrm{Be} + {}^{5}_{\Lambda}\mathrm{He}$ [90]. In Ref. [91], ${}^{15}_{\Xi}$C was assumed to be an excited state with the Ξ^- being in the $1p$ state, and the estimated separation energies of Ξ^- for both ${}^{15}_{\Xi(p)}$C and the ground state of ${}^{12}_{\Xi(s)}$Be were shown to be consistent with the empirical values, i.e. $B_\Xi^{\rm exp}({}^{15}_{\Xi(p)}\mathrm{C}) = 1.11 \pm 0.25$ MeV and $B_\Xi^{\rm exp}({}^{12}_{\Xi(s)}\mathrm{Be}) \approx 5$ MeV. In this case, $B_\Xi({}^{15}_{\Xi(s)}\mathrm{C})$ for the ground state of the ${}^{15}_{\Xi}$C was estimated to be (8.0–9.4) MeV within the RMF calculation [91]. This interpretation concerning the energy-level structure and the binding energy of the Ξ^-–^{14}N system has been confirmed by the recent observation of the twin-Λ hypernuclei (the "IBUKI" event) at the J-PARC E07 experiment [92,93]. In our B–B interaction model, $g_{\sigma^*\Xi^-}$ is taken to be 4.0, for which one obtains $B^{\rm th}_\Xi({}^{15}_{\Xi(s)}\mathrm{C}) = 8.1$ MeV and $B^{\rm th}_\Xi({}^{12}_{\Xi(s)}\mathrm{Be}) = 5.1$ MeV, which are consistent with the empirical values.

The remaining parameter for the σ^*–Σ^- coupling, $g_{\sigma^*\Sigma^-}$, is simply set to be zero since there is little experimental information on the Σ hypernuclei. As seen in the numerical result (Sect. 7.2),

Table 1. The coefficients b and c in the σ self-interaction potential $U_\sigma(\sigma)$ and the meson masses m_a ($a = \sigma, \sigma^*, \omega, \rho, \phi$) used in our RMF model. See the text for details.

b	c	m_σ (MeV)	m_{σ^*} (MeV)	m_ω (MeV)	m_ρ (MeV)	m_ϕ (MeV)
0.008659	−0.002421	400	975	783	769	1020

Table 2. The meson–baryon coupling constants g_{aB} ($a = \sigma, \sigma^*, \omega, \rho, \phi$ and $B = \mathrm{N}, \Lambda, \Sigma^-, \Xi^-$) used in our RMF model.

	N	Λ	Σ^-	Ξ^-
σ	6.39	3.84	2.28	1.94
σ^*	0	7.2	0	4.0
ω	8.72	$\frac{2}{3}g_{\omega N}$	$\frac{2}{3}g_{\omega N}$	$\frac{1}{3}g_{\omega N}$
ρ	4.27	0	$2g_{\rho N}$	$g_{\rho N}$
ϕ	0	$-\frac{\sqrt{2}}{3}g_{\omega N}$	$-\frac{\sqrt{2}}{3}g_{\omega N}$	$-\frac{2\sqrt{2}}{3}g_{\omega N}$

the Σ^- hyperons are not mixed over the relevant densities due to the strong repulsion of the $V_{\Sigma^-}^N$. Therefore, it may safely be said that the simplification $g_{\sigma^*\Sigma^-} = 0$ little affects the results in this paper. It is to be noted that $g_{\sigma^* Y}$ ($Y = \Lambda, \Sigma^-, \Xi^-$) is also related to the s-wave K–B scalar attraction in the ME scheme [see Eq. (49) in Sect. 6.1].

Together with these coupling constants, the meson masses are taken to be $m_\sigma = 400\,\mathrm{MeV}$, $m_{\sigma^*} = 975\,\mathrm{MeV}$, $m_\omega = 783\,\mathrm{MeV}$, $m_\rho = 769\,\mathrm{MeV}$, and $m_\phi = 1020\,\mathrm{MeV}$. The parameters relevant to the meson–baryon interaction used in our RMF model are listed in Tables 1 and 2. In our approach, the parameters such as the meson–baryon coupling constants are fixed in conformity with empirical results, so that these parameters necessarily include experimental and model-dependent uncertainties. Recently, complementary approaches, where large variation of the parameter space is considered with Bayesian analysis by the use of the multi-messenger observations, have been carried out by many authors [94–96].

5. Energy expression in the CI scheme

5.1 *Effective energy density*

The total Lagrangian density $\mathcal{L}$ in the CI scheme for the description of the $(Y + K)$ phase is given by Eqs. (11), (14), and (15), together with the electron part $\mathcal{L}_e$: $\mathcal{L}=\mathcal{L}_B+\mathcal{L}_M+\mathcal{L}_K+\mathcal{L}_e$. The energy density of the $(Y + K)$ phase, $\mathcal{E}$ ($= \mathcal{E}_B + \mathcal{E}_M + \mathcal{E}_K + \mathcal{E}_e$), is obtained from the ground-state expectation value of the Hamiltonian density, $\mathcal{H} = \mathcal{H}_B + \mathcal{H}_M + \mathcal{H}_K + \mathcal{H}_e$, with

$$\mathcal{H}_B = \sum_b (\partial\mathcal{L}_B/\partial\dot{\psi}_b)\dot{\psi}_b - \mathcal{L}_B, \tag{18a}$$

$$\mathcal{H}_M = \sum_m (\partial\mathcal{L}_M/\partial\dot{\varphi}_m)\dot{\varphi}_m - \mathcal{L}_M, \tag{18b}$$

$$\mathcal{H}_K = (\partial\mathcal{L}_K/\partial\dot{K}^-)\dot{K}^- + (\partial\mathcal{L}_K/\partial\dot{K}^+)\dot{K}^+ - \mathcal{L}_K, \tag{18c}$$

$$\mathcal{H}_e = (\partial\mathcal{L}_e/\partial\dot{\psi}_e)\dot{\psi}_e - \mathcal{L}_e, \tag{18d}$$

where φ_m ($= \sigma, \sigma^*, \omega_0, R_0, \phi_0$) is the meson field mediating the B–B interaction, and ψ_e the electron field. From Eqs. (18a) and (7), one obtains

$$\mathcal{E}_B = \sum_{b=p,n,\Lambda,\Sigma^-,\Xi^-} \left\{ \frac{2}{(2\pi)^3} \int_{|\mathbf{p}|\le p_F(b)} d^3|\mathbf{p}|(|\mathbf{p}|^2 + \widetilde{M}_b^{*2})^{1/2} + \rho_b \left(g_{\omega b}\omega_0 + g_{\rho b}\hat{I}_3^{(b)} R_0 + g_{\phi b}\phi_0 \right) \right\}, \tag{19}$$

where $p_F(b)$ is the Fermi momentum of baryon b. From Eqs. (18b) and (15), one obtains

$$\mathcal{E}_M = \frac{1}{2}m_\sigma^2\sigma^2 + U(\sigma) + \frac{1}{2}m_{\sigma^*}^2\sigma^{*2} - \frac{1}{2}m_\omega^2\omega_0^2 - \frac{1}{2}m_\rho^2 R_0^2 - \frac{1}{2}m_\phi^2\phi_0^2. \tag{20}$$

The kaon part of the energy density, $\mathcal{E}_K$, is expressed from Eq. (18c) as

$$\mathcal{E}_K = \mu_K \rho_{K^-} - \mathcal{L}_K, \tag{21}$$

where the first term is obtained by rewriting the first two terms on the right-hand side of Eq. (18c) using the time dependence of the classical kaon field, $\dot{K}^\pm = \pm i\mu_K K^\pm$, which follows from Eq. (1) [1,97], and the number density of kaon condensates,

$$\rho_{K^-} = -iK^-(\partial\mathcal{L}_K/\partial\dot{K}^-) + iK^+(\partial\mathcal{L}_K/\partial\dot{K}^+). \tag{22}$$

Substituting Eqs. (1) and (11) into Eq. (22), one obtains

$$\rho_{K^-} = \mu_K f^2 \sin^2\theta + 2f^2 X_0(1-\cos\theta), \tag{23}$$

where the first term is the kaon kinetic part and the second term comes from the s-wave K–B vector interaction. With Eqs. (23) and (11), Eq. (21) reads

$$\mathcal{E}_K = \frac{1}{2}(\mu_K f \sin\theta)^2 + f^2 m_K^2(1-\cos\theta). \tag{24}$$

The electron part, Eq. (18d), is simply written as

$$\mathcal{E}_e \simeq \mu_e^4/(4\pi^2) \tag{25}$$

for the ultra-relativistic electrons.

With Eqs. (5a)–(5d) the effective energy density $\mathcal{E}_{\rm eff}$ (the thermodynamic potential density, which is equal to the sign-reversed total pressure, $-P$) is separated into

$$\mathcal{E}_{\rm eff} = \mathcal{E}_{{\rm eff},B} + \mathcal{E}_{{\rm eff},M} + \mathcal{E}_{{\rm eff},K} + \mathcal{E}_{{\rm eff},e}, \tag{26}$$

where

$$\mathcal{E}_{{\rm eff},B} = \mathcal{E}_B - \sum_{b=p,n,\Lambda,\Sigma^-,\Xi^-} \mu_b\rho_b, \tag{27a}$$

$$\mathcal{E}_{{\rm eff},M} = \mathcal{E}_M, \tag{27b}$$

$$\mathcal{E}_{{\rm eff},K} = \mathcal{E}_K - \mu_K\rho_{K^-} = -\mathcal{L}_K, \tag{27c}$$

$$\mathcal{E}_{{\rm eff},e} = \mathcal{E}_e - \mu_e\rho_e = \mu_e^4/(4\pi^2) - \mu_e\cdot\mu_e^3/(3\pi^2) = -\mu_e^4/(12\pi^2). \tag{27d}$$

5.2 *Classical kaon field equation and equations of motion for meson mean fields*

The classical kaon field equation is obtained as $\partial\mathcal{E}_{\rm eff}/\partial\theta = 0$, which reads

$$\mu_K^2\cos\theta + 2X_0\mu_K - m_K^{*2} = 0 \tag{28}$$

with

$$m_K^{*2} \equiv m_K^2 - \frac{1}{f^2}\sum_{b=p,n,\Lambda,\Sigma^-,\Xi^-} \rho_b^s \Sigma_{Kb}, \tag{29}$$

where ρ_b^s is a scalar density for baryon b:

$$\rho_b^s = \frac{2}{(2\pi)^3}\int_{|\mathbf{p}|\le p_F(b)} d^3\mathbf{p}\frac{\widetilde{M}_b^*}{(|\mathbf{p}|^2+\widetilde{M}_b^{*2})^{1/2}}. \tag{30}$$

The equations of motion for the meson mean fields in the CI scheme are given from $\partial\mathcal{E}_{\rm eff}/\partial\varphi_m = 0$ ($\varphi_m = \sigma, \sigma^*, \omega_0, R_0, \phi_0$). Using Eqs. (19), (20), and (13) one obtains

$$m_\sigma^2\sigma = -\frac{dU_\sigma}{d\sigma} + \sum_{b=p,n,\Lambda,\Sigma^-,\Xi^-} g_{\sigma b}\rho_b^s, \tag{31a}$$

$$m_\sigma^{*2}\sigma^* = \sum_{Y=\Lambda,\Sigma^-,\Xi^-} g_{\sigma^* Y}\rho_Y^s, \tag{31b}$$

$$m_\omega^2\omega_0 = \sum_{b=p,n,\Lambda,\Sigma^-,\Xi^-} g_{\omega b}\rho_b, \tag{31c}$$

$$m_\rho^2 R_0 = \sum_{b=p,n,\Lambda,\Sigma^-,\Xi^-} g_{\rho b}\hat{I}_3^{(b)}\rho_b, \tag{31d}$$

$$m_\phi^2\phi_0 = \sum_{Y=\Lambda,\Sigma^-,\Xi^-} g_{\phi Y}\rho_Y. \tag{31e}$$

The diagrams of the interaction vertices in the CI scheme are depicted in Fig. 1(a) for the nonlinear K–B interaction and the B–m interaction. In the CI scheme, the structure of the s-wave K–B and K–K interactions is uniquely determined from chiral symmetry, and the mesons m do not directly couple to kaons but only to baryons. A many-body effect appears at the σ–B vertex through the coupling of B to the multi-σ mesons ($\propto dU_\sigma/d\sigma$, shown as (i) in Fig. 1(a)).

The ground state energy for the $(Y+K)$ phase is obtained so as to satisfy Eqs. (28), (31), under the charge neutrality condition $\partial\mathcal{E}_{\rm eff}/\partial\mu = 0$, and chemical equilibrium conditions for weak processes, $\partial\mathcal{E}_{\rm eff}/\partial\rho_i = 0 (i = K^-, e^-, p, n, \Lambda, \Sigma^-, \Xi^-)$ with the total baryon number density ρ_B being fixed. From the last conditions the relations between the chemical potentials, $\mu = \mu_K = \mu_e = \mu_n - \mu_p$, $\mu_\Lambda = \mu_n$, $\mu_{\Sigma^-} = \mu_{\Xi^-} = \mu_n + \mu_e$ [Eqs. (5a)–(5d)] are assured. Here, the baryon chemical potential μ_b (for $b = p, n, \Lambda, \Sigma^-, \Xi^-$) is obtained from Eqs. (19), (20), and (24) with the help of Eqs. (12), (13), (23), and (28)–(31) as

$$\mu_b = \partial\mathcal{E}/\partial\rho_b = \left(p_F(b)^2 + \widetilde{M}_b^{*2}\right)^{1/2} + g_{\omega b}\omega_0 + g_{\rho b}\hat{I}_3^{(b)}R_0 + g_{\phi b}\phi_0 - \mu Q_V^b(1-\cos\theta). \tag{32}$$

From Eq. (32), the baryon potential V_b ($b = p, n, \Lambda, \Xi^-, \Sigma^-$) reads

$$V_b = -g_{\sigma b}\sigma - g_{\sigma^* b}\sigma^* + g_{\omega b}\omega_0 + g_{\rho b}\hat{I}_3^{(b)}R_0 + g_{\phi b}\phi_0 - (\Sigma_{Kb} + \mu Q_V^b)(1-\cos\theta). \tag{33}$$

By setting $\rho_Y = 0$ ($Y = \Lambda, \Xi^-, \Sigma^-$), the description of the energy expression for the $(Y+K)$ phase in the CI scheme reduces essentially to the one studied for kaon-condensed phase in neutron star matter without hyperon-mixing [10].

6. Meson exchange (ME) scheme

6.1 *Correspondence between the ME scheme and the CI scheme*

We recapitulate here the meson exchange (ME) scheme for the s-wave K–B interaction [57,67] in comparison with the CI scheme. In the CI scheme, the s-wave K–B scalar interaction is absorbed into the effective baryon mass $\widetilde{M}_b^*$ [Eq. (13)] in the baryon part of the Lagrangian $\mathcal{L}_B$ [Eq. (14)], and the effect of the s-wave K–B scalar interaction on kaons is involved in the effective kaon mass squared m_K^{*2} [Eq. (29)] through the classical kaon field equation in Eq. (28).

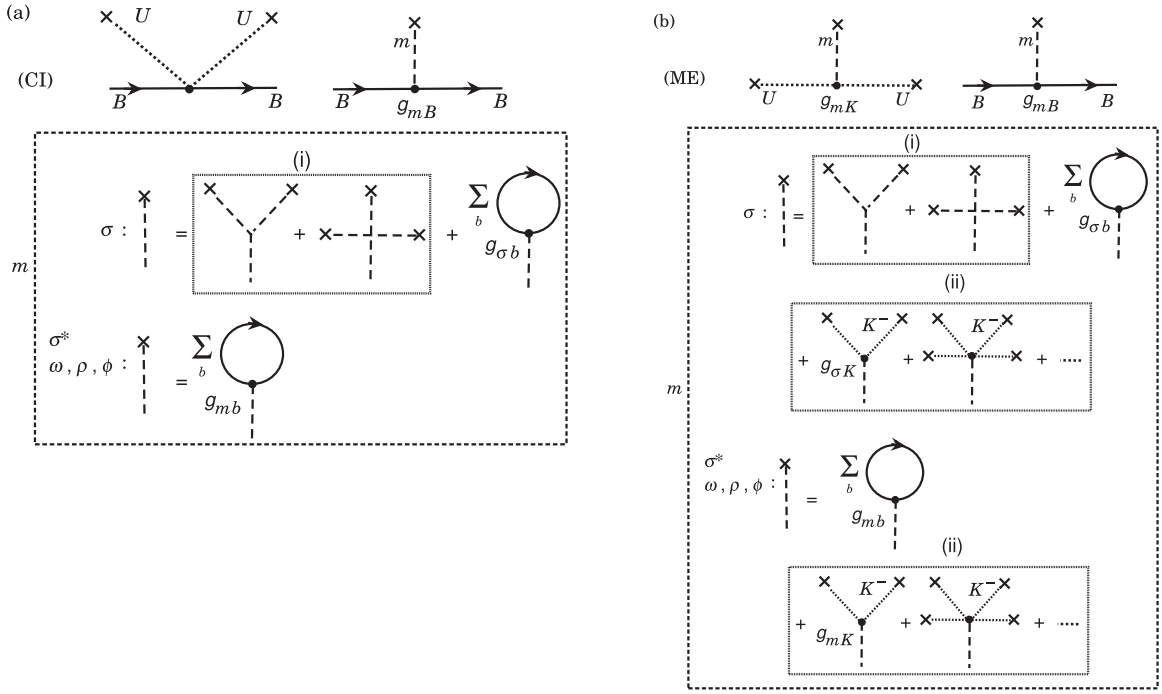

Fig. 1. (a) Diagrams of the interaction vertices in the CI scheme for the nonlinear K–B interaction and the B–m ($m = \sigma, \sigma^*, \omega, \rho, \phi$) interaction. The bold dotted line with a cross ($\times$) stands for the classical nonlinear K^- field U, the solid line for the baryon B, and the dashed line with a cross ($\times$) for the mean field of the meson m ($m = \sigma, \sigma^*$ for the scalar mesons, ω, ρ, ϕ for the vector mesons). The dashed line with no cross at both ends, when connected to the interaction vertices, gives a propagator ($= 1/{m_m}^2$) for the meson m with mass m_m in the Hartree approximation. In the dotted box, the equations of motion for the σ [Eq. (31a)] and those for the other meson fields (σ^*, ω, ρ, ϕ) [Eqs. (31b)–(31e)] are depicted by the diagrams. The diagram (i) comes from the self-interaction term of the multi-σ mesons ($\propto dU_\sigma/d\sigma$). (b) As (a) but in the ME scheme. In the dotted box in the ME scheme, the diagram (ii) stands for the expansion of the kaon source terms in Eqs. (46a)–(46e) in Sect. 6.1 in powers of the kaon field ($\propto \theta$) with the dotted lines.

In the ME scheme, not only baryons but also the kaon field couple only directly with the mesons m ($m = \sigma, \sigma^*, \omega$, ρ, and ϕ) [57,67], and the K–B interaction is mediated by exchange of these mesons. The s-wave K–B scalar interaction in the ME scheme is introduced accordingly as follows. The effective baryon mass [Eq. (13)] appearing in the baryon part of the Lagrangian density $\mathcal{L}_B$ [Eq. (14)] should be modified as

$$\widetilde{M}_b^* \to M_b^*(\mathrm{ME}) = M_b - g_{\sigma b}\sigma - g_{\sigma^* b}\sigma^*, \tag{34}$$

since there is no direct K–B coupling in the ME scheme. Also, the kaon mass squared in the kaon part of the Lagrangian density $\mathcal{L}_K$ [Eq. (11)] is replaced by the effective kaon mass squared $m_K^{*2}(\mathrm{ME})$, i.e.

$$m_K^2 \to m_K^{*2}(\mathrm{ME}) = m_K^2 - 2m_K(g_{\sigma K}\sigma + g_{\sigma^* K}\sigma^*), \tag{35}$$

which should be compared with the m_K^{*2} in the CI scheme [Eq. (29)]. [See also Eq. (48) and subsequent discussion.]

For the s-wave K–B vector interaction, X_0 defined by Eq. (12) appearing in $\mathcal{L}_K$ [Eq. (11)] should be replaced as

$$X_0 \to X_0(\mathrm{ME}) = g_{\omega K}\omega_0 + g_{\rho K}R_0 + g_{\phi K}\phi_0. \tag{36}$$

With the above modification for the K–B scalar and vector interactions, one obtains the Lagrangian density in the ME scheme as $\mathcal{L}(\mathrm{ME})=\mathcal{L}_B(\mathrm{ME})+\mathcal{L}_M+\mathcal{L}_K(\mathrm{ME})+\mathcal{L}_e$ with

$$\mathcal{L}_B(\mathrm{ME}) = \sum_{b=p,n,\Lambda,\Sigma^-,\Xi^-} \overline{\psi_b}(i\gamma^\mu D_\mu^{(b)} - M_b^*(\mathrm{ME}))\psi_b, \tag{37}$$

$$\mathcal{L}_K(\mathrm{ME}) = \frac{1}{2}(f\mu_K \sin\theta)^2 - f^2 m_K^{*2}(\mathrm{ME})(1-\cos\theta) + 2\mu_K X_0(\mathrm{ME}) f^2(1-\cos\theta). \tag{38}$$

The energy density in the ME scheme naturally follows from $\mathcal{L}(\mathrm{ME})$: $\mathcal{E}(\mathrm{ME}) = \mathcal{E}_B(\mathrm{ME})+\mathcal{E}_M+\mathcal{E}_K(\mathrm{ME})+\mathcal{E}_e$, with

$$\mathcal{E}_B(\mathrm{ME}) = \sum_{b=p,n,\Lambda,\Sigma^-,\Xi^-} \left\{ \frac{2}{(2\pi)^3}\int_{|\mathbf{p}|\le p_F(b)} d^3|\mathbf{p}| \left(|\mathbf{p}|^2 + (M_b^*(\mathrm{ME}))^2\right)^{1/2} + \rho_b\left(g_{\omega b}\omega_0 + g_{\rho b}\hat{I}_3^{(b)}R_0 + g_{\phi b}\phi_0\right)\right\}, \tag{39}$$

$$\mathcal{E}_K(\mathrm{ME}) = \mu_K \rho_{K^-}(\mathrm{ME}) - \mathcal{L}_K(\mathrm{ME}) = \frac{1}{2}(\mu_K f\sin\theta)^2 + f^2 m_K^{*2}(\mathrm{ME})(1-\cos\theta), \tag{40}$$

where the number density of kaon condensates, $\rho_{K^-}(\mathrm{ME})$, is given from Eq. (22) by the replacements $m_K^2 \to m_K^{*2}(\mathrm{ME})$ [Eq. (35)] and $X_0 \to X_0(\mathrm{ME})$ [Eq. (36)] in $\mathcal{L}_K$ [Eq. (11)]:

$$\rho_{K^-}(\mathrm{ME}) = \mu_K f^2 \sin^2\theta + 2f^2 X_0(\mathrm{ME})(1-\cos\theta). \tag{41}$$

The effective energy density in the ME scheme, $\mathcal{E}_{\mathrm{eff}}(\mathrm{ME})$, is given as

$$\mathcal{E}_{\mathrm{eff}}(\mathrm{ME}) = \mathcal{E}_{\mathrm{eff},B}(\mathrm{ME}) + \mathcal{E}_M + \mathcal{E}_{\mathrm{eff},K}(\mathrm{ME}) + \mathcal{E}_{\mathrm{eff},e}, \tag{42}$$

where

$$\mathcal{E}_{\mathrm{eff},B}(\mathrm{ME}) = \mathcal{E}_B(\mathrm{ME}) - \sum_{b=p,n,\Lambda,\Sigma^-,\Xi^-} \mu_b(\mathrm{ME})\rho_b, \tag{43a}$$

$$\mathcal{E}_{\mathrm{eff},K}(\mathrm{ME}) = \mathcal{E}_K(\mathrm{ME}) - \mu_K\rho_{K^-}(\mathrm{ME}) = -\mathcal{L}_K(\mathrm{ME}). \tag{43b}$$

In Eq. (43a), $\mu_{\mathrm{b}}(\mathrm{ME})$ is the baryon chemical potential in the ME scheme:

$$\mu_b(\mathrm{ME}) = \partial\mathcal{E}(\mathrm{ME})/\partial\rho_b = \left(p_F(b)^2 + M_b^{*2}(\mathrm{ME})\right)^{1/2} + g_{\omega b}\omega_0 + g_{\rho b}\hat{I}_3^{(b)}R_0 + g_{\phi b}\phi_0. \tag{44}$$

Note that the meson part, $\mathcal{E}_{\mathrm{eff},M}$ $(=\mathcal{E}_M)$, and the electron part, $\mathcal{E}_{\mathrm{eff},e}$, are the same as those in the CI scheme.

In accordance with the above modification, the classical kaon field equation reads

$$\mu_K^2\cos\theta + 2X_0(\mathrm{ME})\mu_K - m_K^{*2}(\mathrm{ME}) = 0, \tag{45}$$

which should be compared with the one in the CI scheme, Eq. (28). The equations of motion for the meson mean fields in the ME scheme are modified to

$$m_\sigma^2\sigma = -\frac{dU_\sigma}{d\sigma} + \sum_{b=p,n,\Lambda,\Sigma^-,\Xi^-} g_{\sigma b}\rho_b^s(\mathrm{ME}) + 2f^2 g_{\sigma K} m_K(1-\cos\theta), \tag{46a}$$

$$m_{\sigma^*}^2\sigma^* = \sum_{Y=\Lambda,\Sigma^-,\Xi^-} g_{\sigma^* Y}\rho_Y^s(\mathrm{ME}) + 2f^2 g_{\sigma^* K} m_K(1-\cos\theta), \tag{46b}$$

$$m_\omega^2\omega_0 = \sum_{b=p,n,\Lambda,\Sigma^-,\Xi^-} g_{\omega b}\rho_b - 2f^2 g_{\omega K}\mu_K(1-\cos\theta), \tag{46c}$$

$$m_\rho^2 R_0 = \sum_{b=p,n,\Lambda,\Sigma^-,\Xi^-} g_{\rho b}\hat{I}_3^{(b)}\rho_b - 2f^2 g_{\rho K}\mu_K(1-\cos\theta), \tag{46d}$$

$$m_\phi^2\phi_0 = \sum_{Y=\Lambda,\Sigma^-,\Xi^-} g_{\phi Y}\rho_Y - 2f^2 g_{\phi K}\mu_K(1-\cos\theta), \tag{46e}$$

with

$$\rho_b^s(\mathrm{ME}) = \frac{2}{(2\pi)^3}\int_{|\mathbf{p}|\le p_F(b)} d^3\mathbf{p}\frac{M_b^*(\mathrm{ME})}{(|\mathbf{p}|^2 + M_b^{*2}(\mathrm{ME}))^{1/2}} \tag{47}$$

being the scalar density for baryon b in the ME scheme. Source terms appear in the equations of motion for meson mean fields in the presence of kaon condensates ($\theta > 0$) (the last terms on the right-hand sides of the equations of motion Eqs. (46a)–(46e)), originating from the kaon–meson (K–m) couplings in the ME scheme. In Fig. 1(b), the diagrams of the interaction vertices in the ME scheme for the nonlinear K–m interaction and the B–m interaction are depicted. In the dotted box in the ME scheme, diagram (ii) represents the expansion of the kaon source terms in Eqs. (46a)–(46e) in powers of the kaon field ($\propto \theta$) with the dotted lines.

In the ME scheme, the mesons (m) couple not only to the baryons (B) but also to the kaon field U [Fig. 1(b)], while they couple only to baryons in the CI scheme [Fig. 1(a)]. As a result, two kinds of many-body effects appear on the K–m couplings in the ME scheme: (i) the derivative term of the σ self-interaction potential $U_\sigma(\sigma)$ with respect to the σ [denoted as (i) in Fig. 1(b)], and (ii) the kaon source terms in the equations of motion for the mesons m [denoted as (ii) in Fig. 1(b)]. Both effects (i) and (ii) lead to differences in the quantities associated with kaon properties between the CI and ME schemes. On the other hand, the nonlinear kaon (U)–B interactions in the ME scheme are generated from the components of mesons (m) connected to baryons in the U–m couplings [the second term on the right-hand side of the σ mean field diagram and the first term of the other meson mean fields diagram in Fig. 1(b)], which are identified with the U–B contact interactions in the CI scheme in Fig. 1(a). For instance, the expression of the effective kaon mass squared, $m_K^{*2}(\mathrm{ME})$ [Eq. (35)], is rewritten with the help of Eqs. (46a) and (46b) as

$$\begin{aligned} m_K^{*2}(\mathrm{ME}) = m_K^2 - \frac{1}{f^2}\sum_b \rho_b^s \Sigma_{Kb}(\mathrm{ME}) + 2g_{\sigma K}\frac{m_K}{m_\sigma^2}\frac{dU_\sigma}{d\sigma} \\ - (2fm_K)^2\left\{\left(\frac{g_{\sigma K}}{m_\sigma}\right)^2 + \left(\frac{g_{\sigma^* K}}{m_{\sigma^*}}\right)^2\right\}(1-\cos\theta), \end{aligned} \tag{48}$$

where $\Sigma_{Kb}(\mathrm{ME})$ ($b = p, n, \Lambda, \Sigma^-, \Xi^-$) is defined as

$$\Sigma_{Kb}(\mathrm{ME}) \equiv 2f^2 m_K\left(\frac{g_{\sigma K}g_{\sigma b}}{m_\sigma^2} + \frac{g_{\sigma^* K}g_{\sigma^* b}}{m_{\sigma^*}^2}\right), \tag{49}$$

which is generated from the U–m couplings through exchange of scalar mesons [the second term on the right-hand side of the σ meson diagram and the first term on the right-hand side of the σ^* meson diagram in Fig. 1(b)], and is identified with the kaon–baryon sigma terms [Eq. (10)]. As compared with the effective kaon mass squared in the CI scheme [Eq. (29)], there are two additional terms in the third and last terms on the right-hand side of Eq. (48) in the ME scheme: the derivative term proportional to $dU_\sigma/d\sigma$ ($= bM_N g_{\sigma N}^3\sigma^2 + cg_{\sigma N}^4\sigma^3$), coming from the equaiton of motion of the σ mean field [Eq. (46a)], represents the many-body effect (i) and has a repulsive effect on the effective kaon mass squared, pushing up the lowest kaon energy ω_K as compared with that in the CI scheme (see Sect. 7.1). This many-body effect (i) entails a difference between the CI and ME schemes for quantities associated with kaon properties such as the effective kaon mass even in the normal phase ($\theta = 0$). On the other hand, the last term, coming from the nonlinear kaon field–scalar meson couplings through the source terms of Eqs. (46a) and (46b), represents the many-body effect (ii), and it works attractively in the presence of kaon condensates, leading to a reduction of $m_K^{*2}(\mathrm{ME})$.

To compare X_0, which represents the s-wave K–B vector interaction, between the CI and ME schemes, the expression of X_0(ME) [Eq. (36)] is rewritten with the help of Eqs. (46c)–(46e) as

$$X_0(\mathrm{ME}) = \frac{1}{2f^2}\sum_b Q_V^b \rho_b - 2f^2\mu_K \left\{ \left(\frac{g_{\omega K}}{m_\omega}\right)^2 + \left(\frac{g_{\rho K}}{m_\rho}\right)^2 + \left(\frac{g_{\phi K}}{m_\phi}\right)^2 \right\}(1-\cos\theta), \quad (50)$$

where the first term on the right-hand side of Eq. (50) results from the following constraints among the vector meson–K and vector meson–B coupling constants:

$$2f^2\left(\frac{g_{\omega K}g_{\omega N}}{m_\omega^2} + \frac{g_{\rho K}g_{\rho N}}{m_\rho^2}\right) = 1, \quad (51a)$$

$$2f^2\left(\frac{g_{\omega K}g_{\omega N}}{m_\omega^2} - \frac{g_{\rho K}g_{\rho N}}{m_\rho^2}\right) = \frac{1}{2}, \quad (51b)$$

$$2f^2\left(\frac{g_{\omega K}g_{\omega \Lambda}}{m_\omega^2} + \frac{g_{\phi K}g_{\phi \Lambda}}{m_\phi^2}\right) = 0, \quad (51c)$$

$$2f^2\left(\frac{g_{\omega K}g_{\omega \Sigma^-}}{m_\omega^2} - \frac{g_{\rho K}g_{\rho \Sigma^-}}{m_\rho^2} + \frac{g_{\phi K}g_{\phi \Sigma^-}}{m_\phi^2}\right) = -\frac{1}{2}, \quad (51d)$$

$$2f^2\left(\frac{g_{\omega K}g_{\omega \Xi^-}}{m_\omega^2} - \frac{g_{\rho K}g_{\rho \Xi^-}}{m_\rho^2} + \frac{g_{\phi K}g_{\phi \Xi^-}}{m_\phi^2}\right) = -1. \quad (51e)$$

These constraints are imposed in order that the terms depending on the number densities of baryons in Eq. (50) correspond to the Tomozawa–Weinberg terms prescribed by chiral symmetry. From Eqs. (51a)–(51c), one obtains the kaon–vector meson coupling constants as

$$\begin{aligned} g_{\omega K} &= 3m_\omega^2/(8f^2 g_{\omega N}) = 3.05, \\ g_{\rho K} &= m_\rho^2/(8f^2 g_{\rho N}) = 2.01, \\ g_{\phi K} &= 3\sqrt{2}m_\phi^2/(8f^2 g_{\omega N}) = 7.33, \end{aligned} \quad (52)$$

where the SU(6) relations for the vector meson–baryon coupling constants, $g_{\omega\Lambda} = (2/3)g_{\omega N}$, $g_{\phi\Lambda} = (-\sqrt{2}/3)g_{\omega N}$, have been used (see Sect. 4.2). The values in Eq. (52) should be compared with those obtained with the quark and isospin counting rule, $g_{\omega K} = g_{\omega N}/3 = 2.90$, $g_{\rho K} = g_{\rho N} = 4.27$, and $g_{\phi K} = g_{\rho\pi\pi}/\sqrt{2} = 4.27$ from the SU(6) relation with $g_{\rho\pi\pi} = 6.04$ [67]. It should be noted that the remaining constraints in Eqs. (51d) and (51e) are shown to be automatically fulfilled using the relations in Eq. (52) for the vector meson–kaon couplings together with the SU(6) relations for the vector meson–Σ^- and Ξ^- coupling constants in Eq. (16).

As compared with the X_0 [Eq. (12)] in the CI scheme, the first term in Eq. (50), which is generated from the U–m couplings through exchange of vector mesons [the first term on the right-hand side of the vector meson diagram in Fig. 1(b)], is identified with the one in Eq. (12) corresponding to the Tomozawa–Weinberg term in the CI scheme. In addition, a term appears on the right-hand side of Eq. (50) coming from the nonlinear kaon field–vector meson couplings through the source terms of Eqs. (46c)–(46e) as a many-body effect (ii) in the ME scheme. This term works repulsively in the presence of kaon condensates to weaken the s-wave K–B vector attraction as far as $\mu_K > 0$.

It should be noted that the K–K interaction is inherent in the nonlinear kaon field in the CI scheme. The resulting K–K scattering length agrees with the current algebra prediction, $-m_K/(16\pi f_K^2)$ [98]. On the other hand, in the ME scheme there is an additional contribution to the K–K scattering length arising from the kaon–scalar meson couplings as a positive contri-

bution and the kaon–vector meson couplings as a negative contribution, leading to a negatively overestimated value of the K–K scattering length. Nevertheless, there is still uncertainty about the experimental value of the K–K scattering length. Therefore, throughout this paper we leave the problem associated with the K–K interaction in the case of the ME scheme as it is, until a consistent description of the nonlinear kaon field with the meson exchange picture becomes possible in a future study.

As for the baryon (B)–meson (m) couplings in the ME scheme, the first three terms on the right-hand side of the σ mean field diagram and the first term on the right-hand side of the other meson mean fields diagram in Fig. 1(b) are common to those in Fig. 1(a) in the CI scheme. Further, the B–m couplings through the many-body effect (ii) arising from the kaon source term in the ME scheme [the fourth term on the right-hand side of the σ mean field diagram and the second term on the right-hand side of the other meson mean fields diagram in Fig. 1(b)] are identified with the nonlinear kaon field (U)–B contact interactions in the CI scheme in Fig. 1(a). Therefore, in contrast to the quantities associated with kaon properties, there is no difference for quantities associated with baryons between the CI and ME schemes. For example, the effective baryon mass M_b^*(ME) [Eq. (34)] is shown to be equal to the $\widetilde{M}_b^*$ [Eq. (13)] in the CI scheme, after being rewritten using Eqs. (46a) and (46b) for M_b^*(ME) and Eqs. (31a) and (31b) for $\widetilde{M}_b^*$ together with the "Kb sigma term" Σ_{Kb} (ME) [Eq. (49)].

In a similar way, the baryon chemical potential μ_b(ME) (for $b = p$, n, Λ, Σ^-, Ξ^-) in the ME scheme, which is given by Eq. (44), is shown to be equal to the μ_b [Eq. (32)] in the CI scheme. In order to reach this result, the former is rewritten using Eqs. (46c)–(46e) for the vector mean fields, together with Eq. (51) to identify the Q_V^b in μ_b [Eq. (32)], and the latter is rewritten using Eqs. (31c)–(31e).

In terms of μ_b(ME), the chemical equilibrium conditions for the weak processes are imposed as $\mu = \mu_K = \mu_e = \mu_n(\mathrm{ME}) - \mu_p(\mathrm{ME})$, $\mu_\Lambda(\mathrm{ME}) = \mu_n(\mathrm{ME})$, $\mu_{\Sigma^-}(\mathrm{ME}) = \mu_{\Xi^-}(\mathrm{ME}) = \mu_n(\mathrm{ME}) + \mu_e$. The charge neutrality condition is written as $\rho_p - \rho_{\Sigma^-} - \rho_{\Xi^-} - \rho_{K^-}(\mathrm{ME}) = 0$ with the number density of kaon condensates ρ_{K^-}(ME) [Eq. (41)].

6.2 *Meson–kaon coupling constants in the ME scheme*

In the ME scheme there remain unknown parameters: the scalar meson–kaon coupling constants, $g_{\sigma K}$ and $g_{\sigma^* K}$. As seen from Eq. (49), $g_{\sigma K}$ is related to the Kn sigma term as $g_{\sigma K} = \Sigma_{Kn}(\mathrm{ME}) m_\sigma^2/(2f^2 m_K g_{\sigma N})$ with $g_{\sigma^* N} = 0$. Here, the value of Σ_{Kn}(ME) is adjusted to be (300−400) MeV, the value adopted in the CI scheme. Then, $g_{\sigma K}$ is determined to be $g_{\sigma K} = 0.88$ (1.17) for $\Sigma_{Kn}(\mathrm{ME}) = 300$ MeV (400 MeV). The scalar σ^* meson coupling to kaons is chosen to be $g_{\sigma^* K} = 2.65/2$ from the decay of $f_0(975)$ [16,38].

The scale of the s-wave K–N attractive interaction can be measured by the K^- optical potential U_K defined at $\rho_B = \rho_0$ in SNM. The U_K in the CI scheme and that in the ME scheme are related by $U_K(\mathrm{ME}) = U_K(\mathrm{CI}) + \dfrac{g_{\sigma K}}{m_\sigma^2}\,(dU_\sigma/d\sigma)_{\sigma=\langle\sigma\rangle}$, as shown Eq. (A5). U_K(ME) is pushed up to a larger value than U_K(CI) due to the repulsive contribution from the kaon–multi-σ meson coupling. The parameters relevant to the meson–kaon interaction in the ME scheme of our RMF model are listed in Table 3. Also, the kaon–baryon sigma terms Σ_{Kb} ($b = p$, n, Λ, Σ^-, Ξ^-) and U_K adopted for both the CI and ME schemes are listed in Table 4. In this paper, the two cases of $\Sigma_{Kn} = 300$ MeV and 400 MeV are mainly considered in both CI and ME schemes. Recently, the inclusive missing-mass spectrum of ^{12}C (K^-, p) reactions has been measured by

Table 3. The meson–kaon coupling constants g_{mK} ($m = \sigma, \sigma^*, \omega, \rho, \phi$) used in the ME scheme. The K^- optical potential U_K for symmetric nuclear matter at saturation density is given as $U_K(\mathrm{ME}) \simeq -(g_{\sigma K}\langle\sigma\rangle + g_{\omega K}\langle\omega_0\rangle)$, where $\langle\sigma\rangle$ and $\langle\omega_0\rangle$ are the meson mean fields at $\rho_p = \rho_n = \rho_0/2$. See the text for details.

Σ_{Kn} (MeV)	U_K(ME) (MeV)	$g_{\sigma K}$	$g_{\sigma^* K}$	$g_{\omega K}$	$g_{\rho K}$	$g_{\phi K}$
300	−77	0.88	2.65/2	$3m_\omega^2/(8f^2 g_{\omega N})$	$m_\rho^2/(8f^2 g_{\rho N})$	$3\sqrt{2}m_\phi^2/(8f^2 g_{\omega N})$
400	−87	1.17	2.65/2	(= 3.05)	(= 2.01)	(= 7.33)

Table 4. The "K–baryon sigma term" Σ_{Kb} ($b = p, n, \Lambda, \Sigma^-, \Xi^-$) and K^- optical potential U_K in symmetric nuclear matter at $\rho_B = \rho_0$ for both the CI and ME coupling schemes. Equation (10) [Eq. (49)] is used for Σ_{Kb} in the CI scheme [in the ME scheme]; Eq. (A4) [Eq. (A5)] is used for U_K in the CI scheme [in the ME scheme].

	Σ_{Kn} (MeV)	Σ_{Kp} (MeV)	$\Sigma_{K\Lambda}$ (MeV)	$\Sigma_{K\Sigma^-}$ (MeV)	$\Sigma_{K\Xi^-}$ (MeV)	U_K (MeV)
CI	300	369	380	300	369	−98
	400	469	480	400	469	−118
ME	300	300	266	107	139	−77
	400	400	326	143	169	−87

the J-PARC E05 experiment [99]. The measured spectrum shape has been reproduced with the real part of the $\bar{K}$-nucleus potential depth $U_K = -80$ MeV and with the imaginary part $W_0 = -40$ MeV, while it is difficult to reproduce the spectrum with a very deep potential such as $|U_K| \sim 200$ MeV. As seen in Table 4, our deduced values for the potential depth U_K corresponding to each Σ_{Kn} for the CI and ME schemes are consistent with these experimental implications for the K^- optical potential depth.

7. Onset density of kaon condensation

We discuss the onset of kaon condensation realized from hyperon-mixed matter in both CI and ME schemes based on our model interaction and compare the results of the two schemes.

7.1 *Lowest K^- energy in hyperon-mixed matter in the CI and ME schemes*

We will show, in Sect. 7.2, that hyperon-mixing precedes kaon condensation at lower densities for the allowable range of $\Sigma_{Kn} = (300{-}400)$ MeV. We therefore consider a continuous phase transition from pure hyperon-mixed matter to the $(Y + K)$ phase. At the onset of kaon condensation, the lowest kaon energy $\omega_K(\rho_B)$ at ρ_B meets the kaon chemical potential μ_K, which is equal to the charge chemical potential μ due to chemical equilibrium for weak processes, $n \rightleftharpoons p + K^-$, $n \rightleftharpoons p + e^-(+\bar{\nu}_e)$ [3]. Therefore, the onset density ρ_B^c is given by

$$\omega_K(\rho_B^c) = \mu, \tag{53}$$

where $\omega_K(\rho_B)$ is given as a pole of the kaon propagator at ρ_B, i.e. $D_K^{-1}(\omega_K; \rho_B) = 0$. The kaon inverse propagator is obtained through expansion of the effective energy density $\mathcal{E}_{\mathrm{eff}}$ with respect to the classical kaon field,

$$\mathcal{E}_{\mathrm{eff}}(\theta) = \mathcal{E}_{\mathrm{eff}}(0) - \frac{f^2}{2} D_K^{-1}(\mu; \rho_{\mathrm{B}})\theta^2 + O(\theta^4), \tag{54}$$

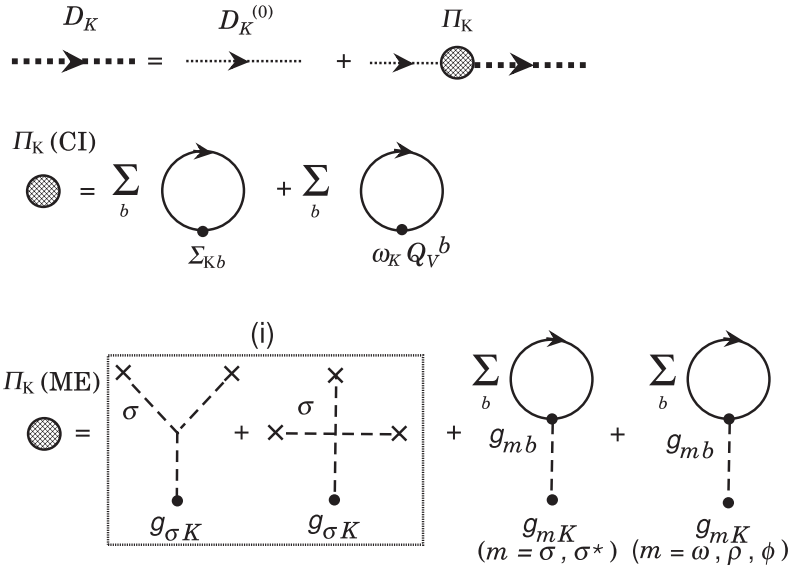

Fig. 2. The diagrams for the kaon propagator D_K (the bold dotted line) and the kaon self-energy $\Pi_K(\omega_K; \rho_B)$ in the CI and ME schemes (the shaded circle). The thin dotted line denotes a free kaon propagator $D_K^{(0)}$ [$=1/(\omega_K^2 - m_K^2)$]. The diagrams for the self-energy in the CI scheme, Π_K(CI), correspond to Eq. (56), and those for the ME scheme, Π_K(ME), to Eq. (57). See the text for details.

which gives

$$D_K^{-1}(\omega_K; \rho_B) = \omega_K^2 - m_K^2 - \Pi_K(\omega_K; \rho_B) \tag{55}$$

with $\Pi_K(\omega_K; \rho_B)$ being the self-energy of kaons. In the CI scheme, it is given by

$$\Pi_K(\omega_K; \rho_B)(\mathrm{CI}) = m_K^{*2} - m_K^2 - 2X_0\omega_K = -\frac{1}{f^2}\sum_{b=p,n,\Lambda,\Sigma^-,\Xi^-}\left(\rho_b^s\Sigma_{Kb} + \omega_K\rho_b Q_V^b\right), \tag{56}$$

which is read off from Eq. (28) by setting $\mu_K \to \omega_K$, $\theta \to 0$, and using Eqs. (12) and (29). In the ME scheme, one has

$$\begin{aligned}\Pi_K(\omega_K; \rho_B)(\mathrm{ME}) &= \left(m_K^{*2}(\mathrm{ME}) - m_K^2 - 2X_0(\mathrm{ME})\omega_K\right)_{\theta\to 0}\\ &= -2m_K(g_{\sigma K}\sigma + g_{\sigma^* K}\sigma^*) - 2\omega_K(g_{\omega K}\omega_0 + g_{\rho K}R_0 + g_{\phi K}\phi_0)\\ &= 2g_{\sigma K}\frac{m_K}{m_\sigma^2}\frac{dU_\sigma}{d\sigma} - \frac{1}{f^2}\sum_{b=p,n,\Lambda,\Sigma^-,\Xi^-}\left(\rho_b^s\Sigma_{Kb}(\mathrm{ME}) + \omega_K\rho_b Q_V^b\right),\end{aligned} \tag{57}$$

where the second and third lines on the right-hand side are obtained from the first line using Eqs. (35) and (36) or Eqs. (48) and (50), respectively. The diagrams for the kaon propagators D_K in the CI and ME schemes are shown in Fig. 2. The dotted line represents kaons and the solid line the baryon b ($= p$, n, Λ, Σ^-, Ξ^-). In the ME scheme, the dashed line represents the σ meson. Comparing Eqs. (56) and (57), one can see that the kaon–multi-σ meson coupling, stemming from the $dU_\sigma/d\sigma$ in the ME scheme denoted as (i), induces an additional repulsive term in the kaon self-energy with nonlinear density dependence, which is absent in the case of the CI scheme.

7.2 *Numerical results for the onset density of kaon condensation realized from hyperon-mixed matter*

In Fig. 3, the lowest kaon energy ω_K is shown as a function of baryon number density ρ_B for the CI case (solid lines) and the ME case (dashed lines). The bold lines (thin lines) are for $\Sigma_{Kn} =$

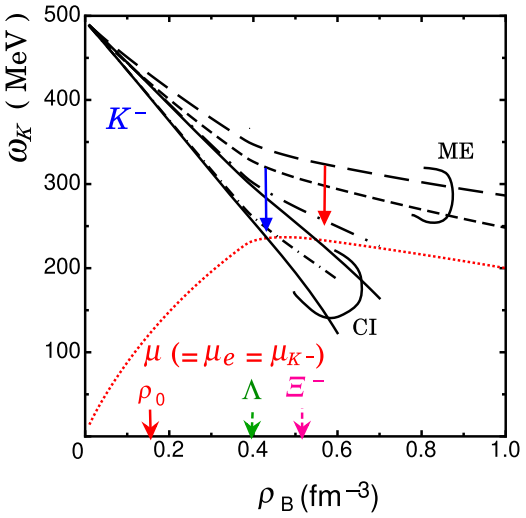

Fig. 3. The lowest kaon energy ω_K as a function of baryon number density ρ_B for the CI case (solid lines) and the ME case (dashed lines). The bold lines (thin lines) are for $\Sigma_{Kn} = 300$ MeV ($\Sigma_{Kn} = 400$ MeV). The dependence of the charge chemical potential μ ($= \mu_e = \mu_{K^-}$) on ρ_B is also shown by the dotted line. See the text for details.

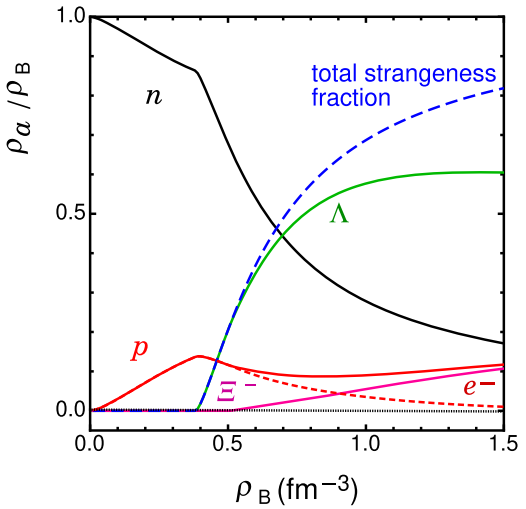

Fig. 4. The particle fractions in pure hyperon-mixed matter with $\theta = 0$ as a function of the baryon number density ρ_B. The total strangeness fraction (the dashed line) is given by $(\rho_\Lambda + 2\rho_{\Xi^-})/\rho_B$.

300 MeV ($\Sigma_{Kn} = 400$ MeV). The dependence of the charge chemical potential μ ($= \mu_e = \mu_{K^-}$) on ρ_B is also shown by the dotted line.

In the CI scheme, the energy ω_K decreases almost linearly with ρ_B from the mass in the vacuum to a value of $O(200\,\text{MeV})$ at $\rho_B = 0.6\,\text{fm}^{-3}$ ($0.5\,\text{fm}^{-3}$) for $\Sigma_{Kn} = 300$ MeV (400 MeV). The onset density of kaon condensates is read as $\rho_B^c(K^-) = 0.548\,\text{fm}^{-3}$ ($= 3.58\rho_0$) for $\Sigma_{Kn} =$ 300 MeV and $\rho_B^c(K^-) = 0.433\,\text{fm}^{-3}$ ($= 2.83\rho_0$) for $\Sigma_{Kn} = 400$ MeV. For reference, we show particle fractions in pure hyperon-mixed matter (θ set to zero) as a function of ρ_B in Fig. 4. In pure hyperon-mixed matter, Λ hyperons start to be mixed in nucleon matter at $\rho_B = \rho_B^c(\Lambda) =$ $0.384\,\text{fm}^{-3}$ ($= 2.51\rho_0$), and subsequently Ξ^- hyperons appear at a higher density $\rho_B = \rho_B^c(\Xi^-)$ $= 0.508\,\text{fm}^{-3}$ ($= 3.32\rho_0$). It is to be noted that Σ^- hyperons are not mixed over the relevant den-

sities, since the potential $V_{\Sigma^-}^N(\rho_0)$ is taken to be strongly repulsive and Ξ^- hyperons are mixed in place of Σ^- hyperons.

As the number density of Λ hyperons increases with $\rho_{\rm B}$, the number densities of proton and electron decrease through the weak process, $p + e^- \to \Lambda + \nu_e$, keeping with $\rho_p = \rho_e$, so that the charge chemical potential μ [$= \mu_e = (3\pi^2\rho_e)^{1/3}$] decreases as $\rho_{\rm B}$ increases after the onset density of the Λ hyperons. Similar to the Λ-mixing case, mixing of Ξ^- hyperons suppresses μ as $\rho_{\rm B}$ increases, through $\Lambda + e^- \to \Xi^- + \nu_e$, as seen in Fig. 4. As a result, the onset density $\rho_{\rm B}^c(K^-)$ is pushed up to a higher density in hyperon-mixed matter as compared with that realized from neutron star matter without hyperon mixing [14,16]. For $\Sigma_{Kn} = 300$ MeV, kaon condensation occurs at a higher density than the onset density of the Ξ^- mixing. For $\Sigma_{Kn} = 400$ MeV, the lowest kaon energy ω_K is smaller than that for the case of $\Sigma_{Kn} = 300$ MeV at a given density due to stronger K–B scalar attraction, and kaon condensation occurs at a density just after the onset density of the Λ mixing and before the density at which the Ξ^- mixing starts.

In the ME scheme, the lowest kaon energy ω_K (the dashed line) lies higher than in the CI scheme (the solid line). The main difference in ω_K between the CI and ME schemes stems from the kaon–multi-σ meson coupling term from (i) [the first term in the third line on the right-hand side of Eq. (57)], which works to increase the energy ω_K as compared with the CI scheme case. For comparison, the lowest kaon energy obtained after this term is subtracted, denoted as ω_K' below, is shown as a function of $\rho_{\rm B}$ by the bold (thin) dash-dotted lines for $\Sigma_{Kn} = 300$ MeV (400 MeV) in Fig. 3. The energy ω_K' is almost equal to the energy ω_K in the CI scheme for $\rho_{\rm B} \lesssim \rho_{\rm B}^c(\Lambda)$. For $\rho_{\rm B} \gtrsim \rho_{\rm B}^c(\Lambda)$, the mixing of Λ leads to a reduction of the K–Λ scalar attraction in the ME scheme as compared with the CI scheme due to the relation $\Sigma_{K\Lambda}({\rm ME}) < \Sigma_{K\Lambda}$ (CI) (see Table 4). Thus, the decrease in ω_K' with $\rho_{\rm B}$ becomes moderate in the presence of Λ hyperons, as does the energy ω_K in the ME scheme. As a result, the energy ω_K in the ME scheme does not cross the charge chemical potential μ over the relevant densities for the standard values of $\Sigma_{Kn} = (300{-}400)$ MeV, so that kaon condensation does not occur over the relevant densities. In our previous works based on the ME scheme, kaon condensation in the hyperon-mixed matter appears at $\rho_{\rm B} \sim 3.3\rho_0$ for $U_K = -120$ MeV [67], which, however, corresponds to a large Kn sigma term, i.e. $\Sigma_{Kn}({\rm ME}) = 754$ MeV, estimated from Eq. (49). In this case the repulsive effect from (i) is compensated by huge attraction given by the s-wave K–B scalar interaction. In most of the other works in the ME scheme with the NLSI scalar potential U_σ, kaon condensation in hyperon-mixed matter appears only for large kaon optical potential depth, $|U_K| \gtrsim 120$ MeV.

The many-body effect (i) appearing solely in the ME scheme depends on the specific form of $U_\sigma(\sigma)$, which is phenomenologically introduced in order to reproduce the empirical value of the incompressibility of nuclear matter at saturation density ($K = 240$ MeV).

In another example of the many-body effects (i), the nonlinear potential of the ω meson, $c(\omega^\mu\omega_\mu)^2/4$, which is introduced to reproduce properties of stable and unstable nuclei systematically in the RMF models [100], would modify the K–B vector interaction, leading to an extra repulsive term, $-cg_{\omega K}\omega_0^3/m_\omega^2$, in the expression for X_0(ME) in Eq. (36). Also, inclusion of the ω–ρ meson coupling term $\lambda(\omega^\mu\omega_\mu)(\vec{R}^\mu \cdot \vec{R}_\mu)$ [101,102], which affects the symmetry energy $S(\rho_0)$ and its slope L at $\rho_{\rm B} = \rho_0$, would lead to both repulsive and attractive contributions to X_0, $-2\lambda g_{\omega K}R_0^2\omega_0/m_\omega^2$ and $-2\lambda g_{\rho K}R_0\omega_0^2/m_\rho^2$ ($R_0 < 0$), respectively. Because of arbitrariness of the NLSI terms as shown above, the corresponding many-body terms entering into the kaon self-energy cannot be fixed uniquely.

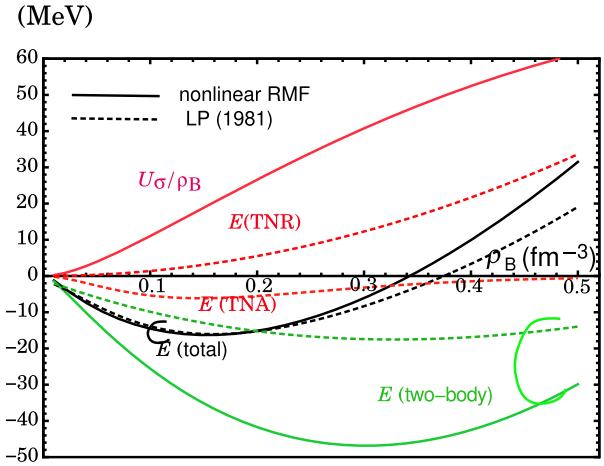

Fig. 5. The total energy per nucleon, E(total), the energy contributions from the NLSI term, E(NLSI) ($= U_\sigma/\rho_B$), and the sum of kinetic and two-body interaction energies, E(two-body), in SNM are shown as functions of ρ_B by the solid lines. For comparison, E(total), E(two-body), and the energy contributions from the three-nucleon repulsion, E(TNR), and three-nucleon attraction, E(TNA), are read from Ref. [103] by the dotted lines. See the text for details.

8. Role of the nonlinear self-interacting term as many-baryon forces

We have shown that the difference in kaon dynamics in dense matter between the CI and ME schemes is caused by the many-body effects (i) derived from the NLSI term, U_σ in this paper. U_σ itself is introduced commonly in both schemes in order to reproduce the empirical incompressibility in SNM. Here we reconsider the role of the NLSI term as many-baryon forces associated with the saturation mechanisms in SNM. We also examine for the NLSI term a possible origin of the many-baryon repulsion in the context of stiffening the EOS for the $(Y + K)$ phase at high densities.

8.1 *Effects of the NLSI term on saturation mechanisms in the SNM*

The total energy per nucleon, E(total), in SNM is separated as E(total) = [$\mathcal{E}$(two-body) + $\mathcal{E}$(NLSI)]/ρ_B, with

$$\begin{aligned}\mathcal{E}(\text{two-body}) &= \sum_{N=p,n}\frac{2}{(2\pi)^3}\int_{|\mathbf{p}|\le p_F} d^3|\mathbf{p}|(|\mathbf{p}|^2+M_N^{*2})^{1/2}\\ &\quad+\frac{1}{2}m_\sigma^2\sigma^2+\frac{1}{2}m_{\sigma^*}^2\sigma^{*2}+\frac{1}{2}m_\omega^2\omega_0^2+\frac{1}{2}m_\rho^2R_0^2+\frac{1}{2}m_\phi^2\phi_0^2,\\ \mathcal{E}(\text{NLSI}) &= U_\sigma,\end{aligned} \tag{58}$$

where p_F is the Fermi momentum of the nucleon in SNM, $p_F = (3\pi^2\rho_B/2)^{1/3}$, and M_N^* ($= M_N - g_{\sigma N}\sigma$) the effective nucleon mass. The B–B two-body interactions, stemming from σ, ω, and ρ meson exchange in the RMF, are included in E(two-body). In Fig. 5, E(total), E(two-body) ($= \mathcal{E}$(two-body)/ρ_B), and E(NLSI) ($= U_\sigma/\rho_B$) are shown as functions of ρ_B by the solid lines. Note that these curves are common to both CI and ME schemes. For comparison, E(total), E(two-body), and the energy contributions from the three-nucleon repulsion, E(TNR), and three-nucleon attraction, E(TNA), which are read from the result in Ref. [103] [LP(1981)], are shown by the dotted lines as a reference for the standard nuclear matter calculation with the variational method. In the case of LP(1981), the three-nucleon forces, both TNR and TNA

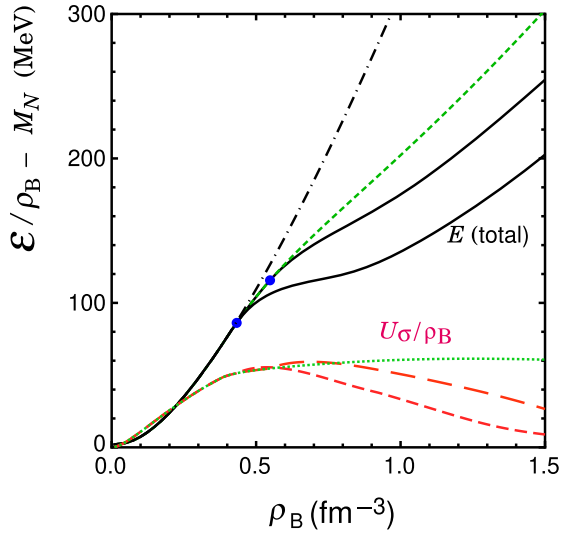

Fig. 6. The energy per baryon, $\mathcal{E}/\rho_B$ (= E(total)), for the $(Y + K)$ phase as a function of ρ_B in the CI scheme for $\Sigma_{Kn} = 300$ MeV and 400 MeV are shown by the bold and thin solid lines, respectively. (The nucleon rest mass is subtracted.) The contribution from the NLSI term, U_σ/ρ_B, is also shown for $\Sigma_{Kn} =$ 300 MeV and 400 MeV by the bold and thin red dashed lines, respectively. For comparison, the one for pure hyperon-mixed matter (set to be $\theta = 0$), which is equal to the energy per baryon in the ME scheme, and the one for pure nucleon matter (set to be $\theta = 0$ and the hyperon-mixing ratio $\rho_Y/\rho_B = 0$) are shown by the green dotted line and the dash-dotted line, respectively. The energy contribution from the NLSI term in the case of the pure hyperon-mixed matter (i.e. in the case of the ME scheme) is also shown in the lower green dotted line.

[E(TNR) = 3.5 MeV and E(TNA) = −6.1 MeV] play the important role of shifting the location of the saturation point due to E(two-body) to the empirical one, where $\rho_B = 0.16\,\text{fm}^{-3}$ and the binding energy = 16.3 MeV. On the other hand, in the present model the NLSI term brings about a large repulsion (20 MeV) at ρ_0 as compared with the TNR in LP(1981). E(NLSI) monotonically increases with ρ_B for $0 < \rho_B \lesssim 0.6\,\text{fm}^{-3}$. Further, a large cancellation between E(NLSI) and E(two-body) maintains saturation of SNM. Therefore, the NLSI term shows quite different aspects quantitatively with respect to saturation mechanisms from those with the standard nuclear matter calculation.

8.2 *Contribution of the NLSI term to the EOS for the $(Y + K)$ phase in the CI scheme*

Following the results on the onset of kaon condensation in Sect. 7.2, we concentrate on the CI scheme to discuss the EOS including the $(Y + K)$ phase and the contribution of the NLSI term to the EOS as many-baryon forces.

In Fig. 6, the energy per baryon, $\mathcal{E}/\rho_B$, in the $(Y + K)$ phase with the nucleon rest mass being subtracted is shown as a function of ρ_B, which is obtained in the CI scheme for $\Sigma_{Kn} =$ 300 MeV and 400 MeV by the bold and thin solid lines, respectively. The contribution from the NLSI term, U_σ/ρ_B, is also shown for $\Sigma_{Kn} = 300$ MeV and 400 MeV by the bold and thin red dashed lines, respectively. In Fig. 7, the pressure P (= $-\mathcal{E}_{\text{eff}}$ [Eq. (26)]) for the $(Y + K)$ phase is shown as a function of the energy density $\mathcal{E}$ in the CI scheme for $\Sigma_{Kn} = 300$ MeV and 400 MeV by the bold and thin solid lines, respectively. For comparison, in both Figs. 6 and 7, the cases for pure hyperon-mixed matter without kaon condensation (set to be $\theta = 0$), which are equal to those obtained in the ME scheme, and for pure nucleon matter (set to be $\theta = 0$ and the

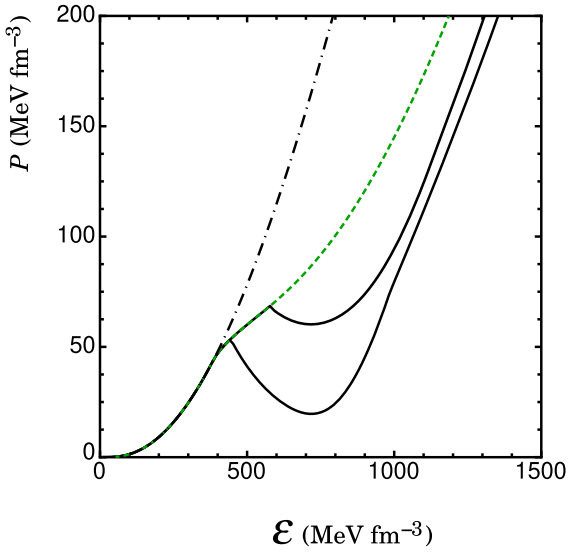

Fig. 7. The pressure P ($= -\mathcal{E}_{\rm eff}$ [Eq. (26)]) in the $(Y + K)$ phase as a function of the energy density $\mathcal{E}$ in the CI scheme, for $\Sigma_{Kn} = 300$ MeV and 400 MeV by the bold and thin solid lines, respectively. The other curves denote the same cases as those for the energies per baryon in Fig. 6.

hyperon mixing ratio $\rho_Y/\rho_{\rm B} = 0$) are also shown by the green dotted line and the dash-dotted line, respectively.

One can see from both figures that once kaon condensation occurs in hyperon-mixed matter, it leads to significant softening of the EOS from the one for pure nucleon matter, since the attractive effect of the s-wave K–B interaction is added as well as the effect of avoiding the N–N repulsion by making the relative number densities of nucleons lower through mixing of hyperons [26]. As seen in Fig. 7, an unstable region, $dP/d\mathcal{E} < 0$, appears as a result of large softening of the EOS in the presence of kaon condensates. In such a density region, the phase equilibrium between the hyperon-mixed phase and the $(Y + K)$ phase should be taken into account under the Gibbs condition, which may lead to an inhomogeneous mixed phase consisting of these phases [105]. It is to be noted that the EOS for the pure nucleon matter (the dash-dotted line) is slightly stiffer than the one according to the A18+δv+UIX* model of Ref. [104].

From Fig. 7, one can read the density dependence of sound velocity c_s [$= (dP/d\mathcal{E})^{1/2}$]. In the nucleon matter, c_s increases monotonically with increase in density. Beyond the onset density of Λ hyperons, c_s abruptly decreases with density, and once kaon condensates appear, the matter becomes unstable, where $c_s^2 < 0$. At high densities, $\rho_{\rm B} \gtrsim 0.7\,{\rm fm}^{-3}$, the $(Y + K)$ phase becomes stable, and c_s increases as density increases. For $\rho_{\rm B} \sim 1.0\,{\rm fm}^{-3}$, $c_s \sim 0.6c$ with c being the speed of light. Over the relevant densities, the causal condition $c_s < c$ is met within the RMF framework.

In Fig. 8 we show the gravitational mass M to radius R relations, obtained as solutions to the Tolman–Oppenheimer–Volkoff equation together with the minimal RMF (MRMF) + NLSI (U_σ) model (denoted as "this work"). The branches including the $(Y + K)$ phase in the core are denoted as the black bold solid line (blue thin solid line) for $\Sigma_{Kn} = 300$ MeV (400 MeV). For comparison, the branch with pure Y-mixed matter (setting $\theta = 0$), which is equal to the one in the ME scheme, is also shown by the green dotted line. The green and yellow bands indicate the restricted regions of the observed masses of PSR J0740+6620 ($2.01\,M_\odot \leq M \leq 2.15\,M_\odot$) [36] and PSR J1810+1744 ($2.09\,M_\odot \leq M \leq 2.17\,M_\odot$) [37], respectively. One can

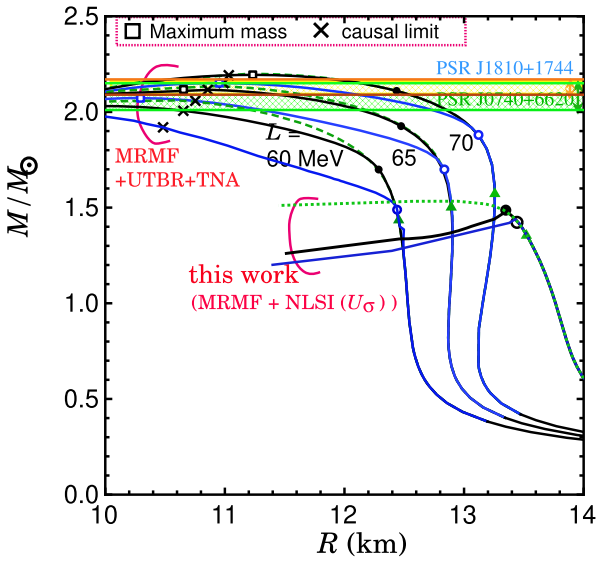

Fig. 8. The gravitational mass M to radius R relations obtained from the minimal RMF (MRMF) + NLSI (U_σ) model (this work). The branches including the $(Y + K)$ phase in the core are denoted as the black bold solid line (blue thin solid lines) for $\Sigma_{Kn} = 300$ MeV (400 MeV). The branch point at which kaon condensates appear in the center of the star is indicated by the filled circle [•] (open circle [○]) in the case of $\Sigma_{Kn} = 300$ MeV (400 MeV). The branch point at which hyperons (Λ) appear is indicated by the filled triangle [▲]. For comparison, the branch with pure Y-mixed matter, where kaon condensates are switched off by setting $\theta = 0$, is also shown by the green dotted line. For reference, the M–R relations obtained by taking into account the universal three-body repulsion (UTBR) and the three-nucleon attraction (TNA) in the MRMF instead of the U_σ (abbreviated as MRMF+UTBR+TNA), taken from Ref. [68], are shown for the slope L of the symmetry energy, $L = (60, 65, 70)$ MeV. The meanings of the curves and symbols (•, ○, ▲) are the same as those for the (MRMF+NLSI) model. In addition, the maximum mass point for each branch including the $(Y + K)$ phase is indicated by the open square [□], and the cross point [×] corresponds to the causal limit at which the sound velocity exceeds the speed of light in the case of the (MRMF+UTBR+TNA) model.

see that the maximum gravitational mass including the $(Y + K)$ phase is (1.44–1.49) $M_\odot$ for $\Sigma_{Kn} = (300-400)$ MeV, and is far below the observational masses of recent massive neutron stars [36,37]. Further, the branches including the $(Y + K)$ phase in the center of the star are unstable, reflecting the large softening of the EOS in the presence of kaon condensates as shown in Fig. 7.

In Fig. 6, the energy contribution from the NLSI term, E(NLSI) ($= U_\sigma/\rho_B$), is also shown for $\Sigma_{Kn} = 300$ MeV and 400 MeV by the bold and thin red dashed lines, respectively. The E(NLSI) in the case of the pure hyperon-mixed matter (i.e. in the case of the ME scheme) is also shown in the lower green dotted line. E(NLSI), which should be relevant to the properties of the SNM around ρ_0, increases with density up to $\rho_B \sim 0.6\,\mathrm{fm}^{-3}$. In the case of the $(Y + K)$ phase, however, the energy contribution from the NLSI term turns to decreasing beyond the density $\rho_B = (0.6-0.7)\,\mathrm{fm}^{-3}$, and the total energy per baryon is dominated by the two-body B–B interaction. In the case of pure hyperon-mixed matter, E(NLSI) becomes saturated around $\rho_B \sim 1\,\mathrm{fm}^{-3}$ and has a minor contribution to the total energy per baryon. Thus, in the context of stiffening the EOS at high densities, the NLSI term is not relevant to the origin of the extra repulsive energy at high densities leading to the solution to the hyperon puzzle. Since the validity of applying such NLSI terms to high densities cannot be assured beyond the phenomenological introduction

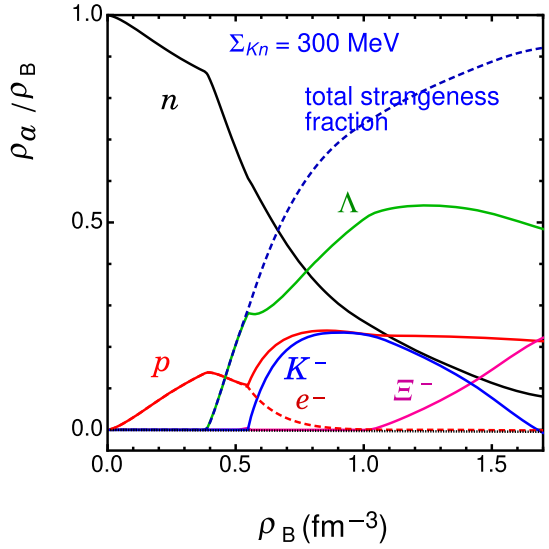

Fig. 9. The particle fractions in the $(Y + K)$ phase as functions of baryon number density ρ_B for $\Sigma_{Kn} =$ 300 MeV. The total strangeness fraction is defined by $(\rho_{K^-} + \rho_\Lambda + 2\rho_{\Xi^-})/\rho_B$.

around ρ_0 for the properties of SNM, the many-body effects appearing in the kaon self-energy in the ME scheme should not be considered as physically solid.

9. Properties of the $(Y + K)$ phase in the CI scheme

Here we summarize the main properties of the $(Y + K)$ phase, namely the density dependence of particle fractions and hyperon potentials in the CI scheme with the (MRMF+NLSI) model, and the self-suppression effect of the s-wave K–B attraction unique to the case of kaon condensation in the RMF framework [10]. These features may be common features in the presence of kaon condensates in the relativistic models.

9.1 *Particle fractions*

The particle fractions ρ_a/ρ_B $(a = p, n, \Lambda, \Xi^-, K^-, e^-)$ in the $(Y + K)$ phase are shown as functions of ρ_B for $\Sigma_{Kn} = 300$ MeV and 400 MeV in Figs. 9 and 10, respectively. For reference, those for the pure hyperon-mixed matter (i.e. in the case of the ME scheme) are shown in Fig. 4.

One can see some common behaviors with respect to the density dependence of particle fractions for both cases, $\Sigma_{Kn} = 300$ MeV and 400 MeV. (I) The fraction of Λ hyperons monotonically increases with density for both cases until kaon condensates appear at $\rho_B^c(K^-)$. Just after the onset of kaon condensation, the growth rate of the Λ fraction with density is slightly suppressed, but it soon recovers to a monotonic increase with density. On the other hand, Ξ^- hyperons appear just before the onset of kaon condensation $[\rho_B^c(\Xi^-) (= 0.508\,\text{fm}^{-3}) < \rho_B^c(K^-)$ $(= 0.548\,\text{fm}^{-3})]$ for $\Sigma_{Kn} = 300$ MeV, but the fraction is tiny, $\rho_{\Xi^-}/\rho_B \lesssim 5 \times 10^{-3}$, around the density $\rho_B = \rho_B^c(\Xi^-)$. For $\Sigma_{Kn} = 400$ MeV, the onset of kaon condensation precedes the Ξ^--mixing. In both cases of Σ_{Kn}, the Ξ^--mixing ratio vanishes once kaon condensates appear until the Ξ^- appears again at higher densities $\rho_B \geq \rho_B^c(\Xi^-$ in $K^-)$, where $\rho_B^c(\Xi^-$ in $K^-)$ is the onset density of the Ξ^- hyperons in the presence of kaon condensates $[\rho_B^c(\Xi^-$ in $K^-) = 1.03\,\text{fm}^{-3}$ $(= 6.73\rho_0)$ for $\Sigma_{Kn} = 300$ MeV and $\rho_B^c(\Xi^-$ in $K^-) = 0.920\,\text{fm}^{-3}$ $(= 6.01\rho_0)$ for $\Sigma_{Kn} = 400$ MeV].

Once kaon condensates appear, they develop together with Λ hyperons as ρ_B increases. However, both kaon condensates and the Λ-mixing ratio gradually decrease as the Ξ^-- mixing starts

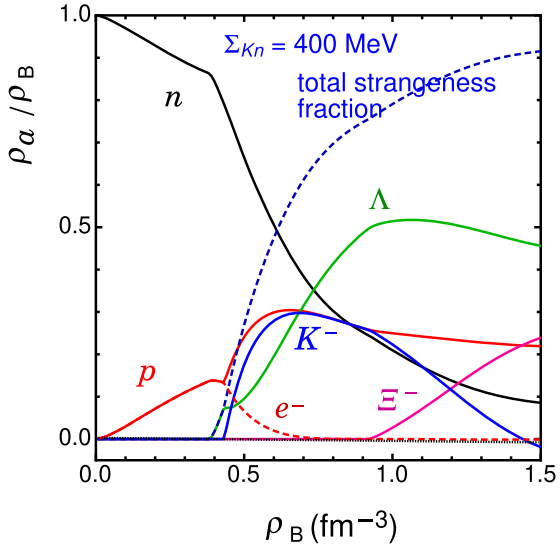

Fig. 10. As Fig. 9, but for $\Sigma_{Kn} = 400$ MeV.

in the fully developed $(Y + K)$ phase at $\rho_B^c(\Xi^-$ in $K^-)$, and further as the fraction of Ξ^- hyperons increases with density. Here one can see a competition between Ξ^- hyperons and kaon condensates. This competitive effect results model-independently from the fact that the number density of kaon condensates, ρ_{K^-} [Eq. (23)], decreases as the number density of Ξ^- hyperons increases due to the negative factor Q_V^b $(= -1$ for Ξ^- hyperons) in the function X_0 [Eq. (12)], which is uniquely assigned as a consequence of chiral symmetry.

(II) The electron fraction is suppressed after the appearance of Λ hyperons or kaon condensates. In particular, the negative charge carried by electrons is taken over by that of kaon condensates avoiding the cost of degenerate energy of electrons and due to the K^-–B attractive interaction. After the onset of kaon condensation, the charge chemical potential μ $[= (3\pi^2\rho_e)^{1/3}]$ decreases as density increases and has a value of $\mu \lesssim O(m_\pi)$. At density $\rho_B \gtrsim 1.22\,\text{fm}^{-3}$ $(= 7.97\rho_0)$ for $\Sigma_{Kn} = 300$ MeV [$\rho_B \gtrsim 0.960\,\text{fm}^{-3}$ $(= 6.27\rho_0)$ for $\Sigma_{Kn} = 400$ MeV], μ becomes negative, where positrons (e^+) are present in place of electrons.

(III) The proton fraction increases along with the growth of kaon condensates, so that the negative charge carried by kaon condensates is compensated by the positive charge of protons keeping the charge neutrality. The neutron fraction decreases with density following the appearance of protons and hyperons due to baryon number conservation.

Here, the density dependence of the Λ and Ξ^--mixing is reconsidered in terms of the hyperon potentials V_Λ and V_{Ξ^-}. The potential V_Λ is shown as a function of ρ_B by the solid line, together with the value of $(\mu_n - M_\Lambda)$ by the long-dashed line for $\Sigma_{Kn} = 300$ MeV in Fig. 11 and for $\Sigma_{Kn} = 400$ MeV in Fig. 12. For reference, V_Λ and the value of $(\mu_n - M_\Lambda)$ for pure hyperonic matter (set to be $\theta = 0$) are shown by the dotted line and the short-dashed line, respectively. The Λ-mixing condition is given by $\mu_n - M_\Lambda > V_\Lambda$. The filled circle (crossing point of the solid line and the long-dashed line) corresponds to the onset density of the Λ-mixing, $\rho_B^c(\Lambda)$, which is lower than the onset density of kaon condensation, $\rho_B^c(K^-)$ (indicated by the vertical dotted line). In the vicinity of $\rho_B^c(K^-)$, both V_Λ and $(\mu_n - M_\Lambda)$ decrease with density as kaon condensation develops due to the s-wave K–Λ and K–n attractive interactions [the last terms on the right-hand sides of Eqs. (33) and (32)]. The reduction of V_Λ is more remarkable than

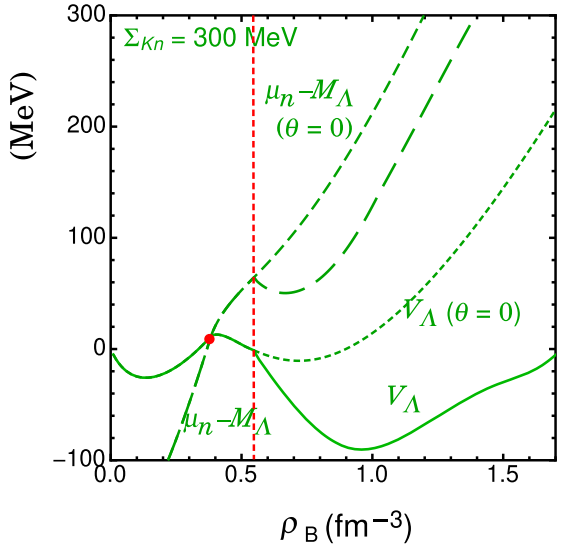

Fig. 11. The Λ potential V_Λ and $(\mu_n - M_\Lambda)$ as functions of baryon number density ρ_B by the solid line and the long-dashed line, respectively, for $\Sigma_{Kn} = 300$ MeV. For reference, those for pure hyperon-mixed matter (set to be $\theta = 0$) are shown by the dotted line and the short-dashed line, respectively. The vertical dotted line indicates the onset density for kaon condensation, $\rho_B^c(K^-)$. See the text for details.

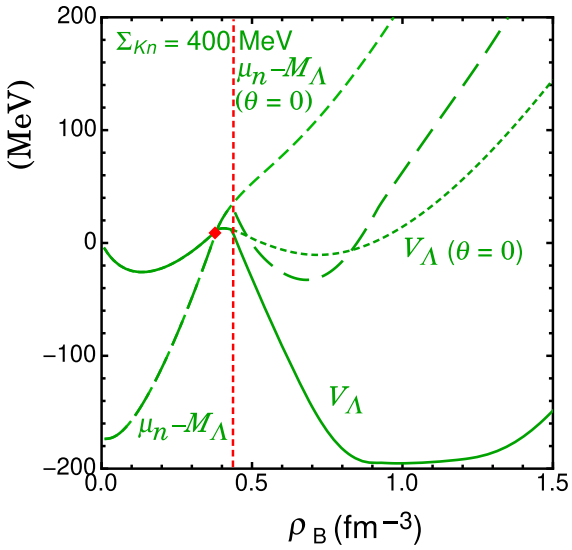

Fig. 12. As Fig. 11, but for $\Sigma_{Kn} = 400$ MeV.

that of $\mu_n - M_\Lambda$, so that the Λ-mixing condition is always met for the relevant densities. Thus, beyond the density $\rho_B^c(\Lambda)$, Λ hyperons continue to be mixed before and after the onset of kaon condensation.

V_{Ξ^-} is shown as a function of ρ_B by the solid line, together with the value of $(\mu_n - M_{\Xi^-} + \mu_e)$ by the long-dashed line, for $\Sigma_{Kn} = 300$ MeV in Fig. 13 and for $\Sigma_{Kn} = 400$ MeV in Fig. 14. V_{Ξ^-} and the value of $(\mu_n - M_{\Xi^-} + \mu)$ for pure hyperon-mixed matter are also shown by the dotted line and the short-dashed line, respectively. Beyond the onset density $\rho_B^c(K^-)$, both V_{Ξ^-} and μ_n decrease with density as kaon condensation develops, since the s-wave K–Ξ^- and K–n interactions work attractively [see Eqs. (32) and (33).] However, owing to the decrease in the electron chemical potential μ_e $(= \mu)$ with density, the term $(\mu_n - M_{\Xi^-} + \mu_e)$ decreases more rapidly

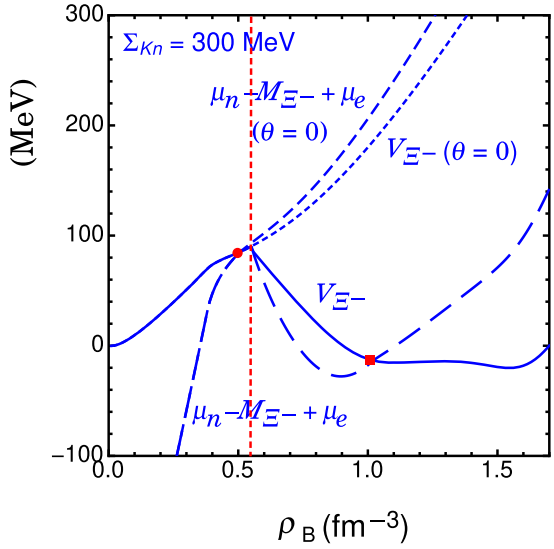

Fig. 13. The Ξ^- potential V_{Ξ^-} and $(\mu_n - M_{\Xi^-} + \mu_e)$ as functions of baryon number density ρ_B by the solid line and the long-dashed line, respectively, for $\Sigma_{Kn} = 300$ MeV. For reference, those for pure hyperon-mixed matter (set to be $\theta = 0$) are shown by the dotted line and the short-dashed line, respectively. The vertical dotted line indicates the onset density for kaon condensation, $\rho_B^c(K^-)$. See the text for details.

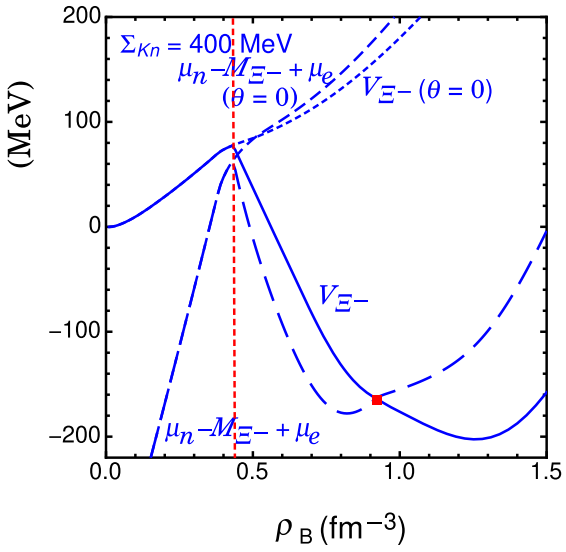

Fig. 14. As Fig. 13, but for $\Sigma_{Kn} = 400$ MeV.

than V_{Ξ^-}. Therefore, the condition for Ξ^--mixing, $\mu_n - M_{\Xi^-} + \mu_e > V_{\Xi^-}$, is not satisfied, i.e. μ_e is not large enough to assist the Ξ^--mixing. For $\Sigma_{Kn} = 300$ MeV, although the Ξ^--mixing starts before kaon condensation sets in, it soon vanishes just after the onset of kaon condensation. At high densities $\rho_B \gtrsim 1.0\,\text{fm}^{-3}$, μ_n increases with density due to the dominant two-body repulsive interaction, and the condition for Ξ^--mixing is satisfied again at $\rho_B \geq \rho_B^c(\Xi^- \text{ in } K^-) = 1.03\,\text{fm}^{-3}$ (the second crossing point of the solid line and the long-dashed line in Fig. 13). For $\Sigma_{Kn} = 400$ MeV, the onset of kaon condensation precedes the Ξ^--mixing, and the Ξ^--mixing does not occur until ρ_B exceeds $\rho_B^c(\Xi^- \text{ in } K^-)$ $(= 0.92\,\text{fm}^{-3}$; Fig. 14).

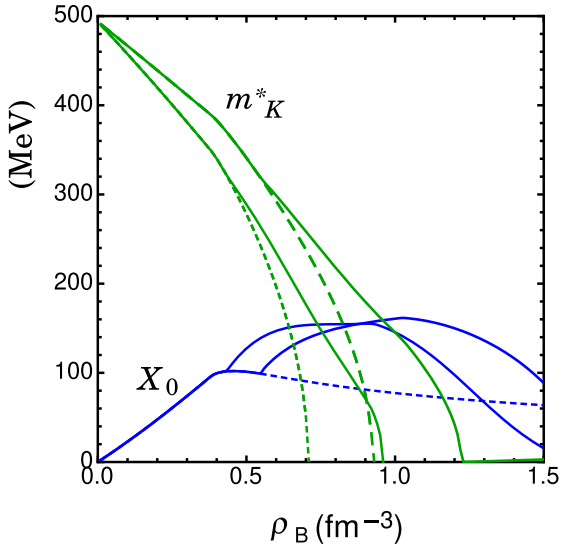

Fig. 15. The density dependence of the effective kaon mass m^*_K given by Eq. (29) and X_0 by Eq. (12) in the $(Y + K)$ phase (solid lines) and in pure hyperon-mixed matter with θ set to be zero (dashed lines). In the case of m^*_K and X_0 in the $(Y + K)$ phase, the bold lines are for $\Sigma_{Kn} = 300$ MeV and the thin lines for $\Sigma_{Kn} = 400$ MeV. In pure hyperonic matter, X_0, responsible for the s-wave K–B vector attraction, does not depend on Σ_{Kn}, so only the thin dashed line is depicted.

It is to be noted that Σ^- hyperons do not appear in the $(Y + K)$ phase over the relevant densities, as is the case with pure hyperonic matter (Fig. 4). The total strangeness fraction, $(\rho_{K^-} + \rho_\Lambda + 2\rho_{\Xi^-})/\rho_B$, increases steadily with ρ_B in accordance with the growth of hyperon-mixing and kaon condensates, and it amounts to 0.9 at $\rho_B \sim 1.5\,\mathrm{fm}^{-3}$ for both cases of $\Sigma_{Kn} =$ 300 MeV and 400 MeV.

9.2 *Self-suppression mechanisms*

Here we discuss the relativistic effects of kaon condensates on the s-wave K–B scalar and vector interactions. In Fig. 15, the density dependence of the effective kaon mass m^*_K given by Eq. (29) and that of X_0 given by Eq. (12) are shown by the solid lines for the $(Y + K)$ phase. For comparison, those for the pure hyperon-mixed matter with θ set to be zero are shown by the dashed lines. In the case of m^*_K and X_0 in the $(Y + K)$ phase, bold lines are for $\Sigma_{Kn} = 300$ MeV and thin lines for $\Sigma_{Kn} = 400$ MeV. In pure hyperonic matter, X_0, responsible for the s-wave K–B vector attraction, does not depend on Σ_{Kn}, so only the thin dashed line is depicted. The difference of m^*_K between the solid and dashed lines stems from the suppression of the scalar density due to the appearance of kaon condensates. Thus, one can see that the *self-suppression mechanism* of the s-wave K–B scalar interaction in the RMF framework becomes remarkable in the presence of kaon condensates [10]: as kaon condensation develops with ρ_B, the effective baryon mass $\widetilde{M}^*_b$ decreases following Eq. (13). The decrease in $\widetilde{M}^*_b$ leads to saturation of the scalar density for baryons, ρ^s_b, at higher densities, which, in turn, results in the suppression of the K–B scalar attraction in the presence of kaon condensates through the term proportional to ρ^s_b in m^*_K [Eq. (29)].

On the other hand, X_0, representing the K–B vector interaction, is enhanced by the appearance of kaon condensates, as seen in Fig. 15. The enhancement of X_0 results mainly from the increase in proton density ρ_p in response to the growth of kaon condensates.

In Ref. [31], the EOS of the $(Y + K)$ phase is considered based on the effective chiral Lagrangian with the nonrelativistic framework for baryons by adding the schematic baryon potential V_b ($b = p, n, \Lambda, \Sigma^-, \Xi^-$) parameterized in terms of the number densities of baryons. It has been shown that the energy gain due to the combined effects of both kaon condensates and the hyperon-mixing is so strong that a local minimum of the energy with respect to $\rho_{\rm B}$ appears, leading to self-bound objects with $(Y + K)$ phase for $\Sigma_{Kn} = 300$ MeV [31]. However, in the present result based on the RMF with the self-contained baryon potential V_b [Eq. (33)], the s-wave K–B scalar interaction is suppressed at high densities due to the self-suppression mechanism as a relativistic effect. As a result, the energy per baryon monotonically increases with $\rho_{\rm B}$ (Fig. 6), and the self-bound star formed of the $(Y + K)$ phase is unlikely to exist.

Although the s-wave K–B scalar attraction is suppressed through the self-suppression mechanism within the relativistic framework, such suppression is not enough to make the EOS stiff so as to be consistent with the recent observations of massive neutron stars [32–37], as stated with reference to Fig. 8 in the case of the MRMF+NLSI (U_σ) model. The previous result based on the MRMF+NLSI (U_σ) model with coupling constants similar to those in the present paper also shows that the maximum gravitational mass is (1.5–1.6) $M_\odot$ for $\Sigma_{Kn} = (300-400)$ MeV [106]. In order to construct a realistic EOS including the $(Y + K)$ phase that is compatible with the recent observations of massive neutron stars, some mechanisms to circumvent both the large attraction due to the s-wave K–B interaction and the energy decrease due to the hyperon-mixing effect are still necessary.

10. Circumventing the problems caused by the NLSI term

With regard to repulsive effects for baryons, the three-body NNN, YNN, YYN, YYY forces have been introduced as the extra repulsion in the case of hyperon-mixed matter [26]. It has been shown that the universal three-body repulsion, derived based on the string junction model by Tamagaki (abbreviated here as UTBR) [107], prevents the EOS from "dramatic softening" due to the hyperon-mixing, and that massive neutron stars as high as 2 $M_\odot$ can be obtained [107,108]. Recently, we introduced the density-dependent effective two-body potentials for the UTBR based on the string-junction model 2 in Ref. [107] together with the phenomenological three-nucleon attraction (TNA), in addition to the MRMF, where baryon interactions are simply composed of the two-body B–B interaction mediated by meson exchange, without recourse to the nonlinear self-interacting σ, ω, or ω–ρ meson-coupling potentials [68]. In this model (MRMF+UTBR+TNA), the UTBR is supposed to be relevant to the short-range part of the B–B interaction, where the quark structure of baryon reveals itself. Therefore, UTBR has been phenomenologically introduced beyond the RMF picture [106], while baryons can be viewd as point-like within the RMF in the intermediate and long-range part of the interaction. This baryon interaction model can describe the saturation properties of the SNM, following each energy contribution from three-nucleon repulsion and attraction, and two-body parts similar to those obtained by conventional nuclear matter theory [103]. It is also emphasized that, once the NLSI term is replaced by the UTBR+TNA, the many-body effects arising from the NLSI term in the ME scheme are removed, and that the kaon self-energy in hyperon-mixed matter ($\theta \to 0$) with such an (MRMF+UTBR+TNA) model is formally equivalent between the CI and ME schemes for the kaon–baryon vertices, even though, in the presence of kaon condensates, there still remains many-body effect (ii) only in the ME scheme [the fourth (second) term on the

right-hand side of Eq. (48) (Eq. (50))] coming from the kaon source terms in the equations of motion for the meson mean fields.

With this baryon interaction model (MRMF+UTBR+TNA) coupled with the effective chiral Lagrangian, we considered the $(Y + K)$ phase in Ref. [68]. It has been shown that softening of the equation of state stemming from both kaon condensation and mixing of hyperons is compensated with the repulsive effect of the UTBR and the relativistic effect for two-body B–B interaction. It has also been shown that the EOS and the resulting mass and radius of compact stars accompanying the $(Y + K)$ phase are consistent with recent observations of massive neutron stars [36,37,50–53]. In Fig. 8, the M–R relations obtained by using the (MRMF+UTBR+TNA) model are shown for the slope L [$\equiv 3\rho_0 (\partial S/\partial \rho_B)_{\rho_B=\rho_0, x=1/2}$] of the symmetry energy $S(\rho_{\rm B})$, $L = (60, 65, 70)$ MeV. The result is taken from Ref. [68]. It should be noted that the unstable region, $c_s^2 = dP/d\mathcal{E} < 0$, which appears in the MRMF+NLSI (U_σ) model, is washed out in the realistic calculation with the MRMF+UTBR+TNA model by taking into account the relevant three-body interactions [68].

11. Summary and concluding remarks

We have compared two coupling schemes, the contact interaction (CI) and meson-exchange (ME) schemes, concerning the K–B and K–K interactions in the effective chiral Lagrangian. We have considered how the onset density of kaon condensation realized from hyperon-mixed matter and the EOS of the $(Y + K)$ phase are affected in these two schemes. The nonlinear self-interacting (NLSI) σ-meson potential $U_\sigma(\sigma)$ has been introduced in both schemes to reduce the incompressibility at saturation density of symmetric nuclear matter. In the ME scheme, there appear many-body effects in the K–B interaction through the kaon–multi-σ-meson coupling stemming from the derivative term, $dU_\sigma/d\sigma$. The kaon–multi-σ-meson coupling term has a sizable repulsive contribution to the kaon energy ω_K. Hence, the onset condition of kaon condensation, $\omega_K = \mu$, is not fulfilled over the relevant baryon densities in the case of the ME scheme unless Σ_{Kn} is taken to be extraordinarily large. In general, the NLSI terms bring about extra terms for the kaon self-energy in the ME scheme beyond the scope of chiral symmetry.

On the other hand, the K–B interaction for the kaon self-energy in the CI scheme is specified by chiral symmetry and free from such ambiguity of many-body effects brought about by the NLSI terms. In this scheme, the onset of kaon condensation occurs at a density $\rho_{\rm B}^c(K^-) =$ (3–4)ρ_0 for the standard values of $\Sigma_{Kn} =$ (300–400) MeV.

In the context of stiffening of the EOS at high densities, the NLSI term is not relevant as the origin of the extra repulsive energy at high densities leading to a solution to the "hyperon puzzle," since the contribution to the repulsive energy gradually decreases with increase in density. Actually, in the case of the CI scheme, the EOS for the $(Y + K)$ phase is considerably softened even with the NLSI term after the appearance of kaon condensates in hyperon-mixed matter.

As stated in Sect. 10, the (MRMF+UTBR+TNA) model [68] reveals a satisfactory picture for saturation of SNM in view of the standard variational nuclear matter theory with the phenomenological three-nucleon forces (TNR and TNA) [103,104]. Moreover, the UTBR, introduced as the effective two-body baryon potential in the model, has a decisive contribution to stiffening of the EOS with the $(Y + K)$ phase at high densities as a solution to the "hyperon puzzle." In these respects, the (MRMF+UTBR+TNA) model is considered to be more natural and plausible than the (MRMF+NLSI) model elucidated in the present paper. As a consequence, the many-body effects (i) originating from the NLSI terms and the resulting extra

terms which make the difference between the CI and ME schemes in the (MRMF+NLSI) model should not be regarded as solid and universal. The results on the comparison of the (MRMF+UTBR+TNA) model and the (MRMF+NLSI) model with specific NLSI terms such as U_σ, quartic terms of the vector ω meson, and ω–ρ meson coupling terms, etc. will be reported in detail elsewhere [109].

In this paper we have concentrated specifically on the NLSI terms in the RMF leading to the difference in kaon dynamics in dense matter between the CI and ME schemes. As another prescription for describing nuclear matter and finite nuclei, density dependence for meson–baryon coupling constants has been taken into account within the RMF framework to be consistent with the result of the self-energy of the Dirac–Brueckner calculation of nuclear matter [110]. Some authors have considered kaon condensation in the ME scheme with density-dependent meson–baryon coupling strengths in place of the NLSI terms [44–46]. In this approach, the formal expression of the kaon self-energy is essentially the same as in the CI scheme, while density dependence of the meson–baryon coupling strengths lead to an extra nonlinear density dependence of the kaon self-energy in addition to the density dependence of the baryon scalar densities.

As another possible repulsion between baryons, the multi-pomeron exchange potential has been considered as an origin of many-body forces [111]. As another example of many-body forces, the BMM, MMM-type diagrams, which follow from the specific counting rule of the meson–baryon diagrams, have been considered within the RMF [112].

Anti-symmetrization effects in the Hartree–Fock approximation for baryons is another issue to be elucidated for construction of a realistic EOS of the $(Y + K)$ phase. In Refs. [113,114] the tensor coupling of vector mesons has been introduced in the RMF for the EOS of hyperon-mixed matter. It has been pointed out that the Fock contribution hinders the appearance of hyperons at middle and high densities, and also suppression of hyperon mixing at high densities. For the $(Y + K)$ phase, the Fock contribution may have a minor effect on the population of kaon condensates, so that kaon condensation may be dominant over hyperons at high densities.

Throughout this paper, hadrons are considered as point-like particles even at high densities, where they are supposed to overlap with each other, and quark degrees of freedom should be explicitly considered. In Refs. [115–117], the hadron phase (hyperon-mixed matter) was connected smoothly to the quark phase in a hadron–quark crossover picture. The resulting EOS has been shown to be stiff enough to have massive stars as much as two solar masses. In this context, kaon condensation may play an important role in both the hadron and quark phases. In particular, kaonic modes may be condensed in the color–flavor locked phase [118–122]. It will be interesting to clarify the relationship between kaon condensation in the hadronic phase and that in the quark phase, and to construct a stiff EOS including the hadron–quark crossover, which may be consistent with recent observations of massive neutron stars.

Acknowledgement

This work is supported in part by the Grant-in-Aid for Scientific Research on Innovative Areas "Nuclear Matter in Neutron Stars Investigated by Experiments and Astronomical Observations." T. Muto acknowledges the financial support by Chiba Institute of Technology.

Appendix A

A1. Estimation of the KN sigma term

We estimate the allowable values of the Kn sigma term, Σ_{Kn}. The "K-baryon sigma term" is defined by

$$\Sigma_{Kb} = \frac{1}{2}(m_u + m_s)\langle b|(\bar{u}u + \bar{s}s)|b\rangle, \tag{A1}$$

where $\langle b|\bar{q}q|b\rangle$ is the quark condensate in the baryon species b ($b = p$, n, Λ, Σ^-, Ξ^- in this paper).

In the chiral perturbation theory, one obtains the $\bar{q}q$ condensates from Eq. (9) using the relations $\langle b|\bar{q}q|b\rangle = \partial M_b/\partial m_q$:

$$\begin{aligned}
\langle p|\bar{u}u|p\rangle &= \langle n|\bar{d}d|n\rangle = -2(a_1 + a_3),\\
\langle p|\bar{d}d|p\rangle &= \langle n|\bar{u}u|n\rangle = -2a_3,\\
\langle p|\bar{s}s|p\rangle &= \langle n|\bar{s}s|n\rangle = -2(a_2 + a_3).
\end{aligned} \tag{A2}$$

Substituting Eq. (A2) into Eq. (A1), one obtains Eq. (10). For instance, the K–neutron σ term is given as $\Sigma_{Kn} = -(a_2 + 2a_3)(m_u + m_s)$.

The quark masses m_i are chosen to be $m_u = 6$ MeV, $m_d = 12$ MeV, and $m_s = 240$ MeV, according to Ref. [1]. Furthermore, the parameters a_1 and a_2 are fixed to be $a_1 = -0.28$, $a_2 = 0.56$ so as to reproduce the empirical octet baryon mass splittings [1]. We fix the remaining parameter a_3 with reference to the standard value of the πN sigma term, $\Sigma_{\pi N} = 45$ MeV, which is extracted from the π–N scattering data [123]. Using Eq. (A2), $\Sigma_{\pi N}$ is written as

$$\Sigma_{\pi N} = \frac{1}{2}(m_u + m_d)\langle N|(\bar{u}u + \bar{d}d)|N\rangle = -(a_1 + 2a_3)(m_u + m_d), \tag{A3}$$

from which one obtains $a_3 = -1.1$. With this value, one obtains $\Sigma_{Kn} = 403$ MeV and $y \equiv 2\langle N|\bar{s}s|N\rangle/\langle N|(\bar{u}u + \bar{d}d)|N\rangle = 2(a_2 + a_3)/(a_1 + 2a_3) = 0.44$, which implies large $\bar{s}s$ condensate in the nucleon.

On the other hand, recent lattice QCD results suggest small $\bar{s}s$ condensate, $y \simeq 0$ [124–126], for which the expressions in Eq. (A2) followed by Eq. (9) based on lowest-order chiral perturbation theory cannot be applied. In this case, assuming $\langle N|\bar{u}u|N\rangle = \langle N|\bar{d}d|N\rangle$ and $\langle N|\bar{s}s|N\rangle = 0$, one obtains $\langle N|\bar{u}u|N\rangle = \Sigma_{\pi N}/(m_u + m_d) = 2.5$ with $\Sigma_{\pi N} = 45$ MeV, and the lower value for Σ_{KN} is estimated as $\Sigma_{KN} = 308$ MeV.

Throughout this paper we consider the two cases of $\Sigma_{Kn} = 300$ MeV and 400 MeV as the standard values, considering the uncertainty of the $\bar{s}s$ condensate in the nucleon.

A2. K^- optical potential

The strengh of the in-medium K–N attraction is simulated by the the K^- optical potential U_K at $\rho_B = \rho_0$ in symmetric nuclear matter. In the CI scheme, it is defined using the K^- self-energy [Eq. (56)]

$$U_K(\mathrm{CI}) \equiv \Pi_K(\mathrm{CI})/(2\omega_K(\rho_B))|_{\rho_p=\rho_n=\rho_0/2} = -\frac{1}{f^2}\left(\rho_0^s \frac{\Sigma_{Kn} + \Sigma_{Kp}}{4\omega_K(\rho_0)} + \frac{3}{8}\rho_0\right) \tag{A4}$$

with the nuclear scalar density ρ_0^s at $\rho_{\rm B} = \rho_0$ in symmetric nuclear matter. In the ME scheme, one obtains, from Eqs. (57) and (A4),

$$U_K(\mathrm{ME}) \equiv \Pi_K(\mathrm{ME})/(2\omega_K(\rho_B))|_{\rho_B=\rho_0} \simeq -(g_{\sigma K}\langle\sigma\rangle_0 + g_{\omega K}\langle\omega_0\rangle_0)$$
$$= U_K(\mathrm{CI}) + \frac{g_{\sigma K}}{m_\sigma^2}\left(\frac{dU_\sigma}{d\sigma}\right)_{\sigma=\langle\sigma\rangle_0}, \tag{A5}$$

where the approximation $\omega_K(\rho_0) \sim m_K$ has been used.

References

[1] D. B. Kaplan and A. E. Nelson, Phys. Lett. **B 175**, 57 (1986).
[2] T. Tatsumi, Prog. Theor. Phys. **80**, 22 (1988).
[3] T. Muto and T. Tatsumi, Phys. Lett. B **283**, 165 (1992).
[4] T. Muto, Prog. Theor. Phys. **89**, 415 (1993).
[5] T. Muto, R. Tamagaki, and T. Tatsumi, Prog. Theor. Phys. Suppl. **112**, 159 (1993). T. Muto, T. Takatsuka, R. Tamagaki, and T. Tatsumi; Prog. Theor. Phys. Suppl. 112, 221 (1993).
[6] H. Fujii, T. Muto, T. Tatsumi, and R. Tamagaki, Nucl. Phys. A **571**, 758 (1994) Phys. Rev. C50, 3140 (1994).
[7] V. Thorsson, M. Prakash, and J. M. Lattimer, Nucl. Phys. A **572**, 693 (1994); **574**, 851 (1994) [erratum].
[8] E. E. Kolomeitsev, D. N. Voskresensky, and B. Kämpfer, Nucl. Phys. A **588**, 889 (1995).
[9] C. -H. Lee, G. E. Brown, D. -P. Min, and M. Rho, Nucl. Phys. A **585**, 401 (1995).
[10] H. Fujii, T. Maruyama, T. Muto, and T. Tatsumi, Nucl. Phys. A **597**, 645 (1996).
[11] K. Tsushima, K. Saito, A. W. Thomas, and S. V. Wright, Phys. Lett. B **429**, 239 (1998); **436**, 453 (1998) [erratum].
[12] T. Tatsumi and M. Yasuhira, Phys. Lett. B **441**, 9 (1998); Nucl. Phys. **A 653**, 133 (1999).
[13] N. K. Glendenning, Astrophys. J. **293**, 470 (1985); N. K. Glendenning, and S. A. Moszkowski; Phys. Rev. Lett. 67, 2414 (1991).
[14] P. J. Ellis, R. Knorren, and M. Prakash, Phys. Lett. B **349**, 11 (1995).
[15] R. Knorren, M. Prakash, and P. J. Ellis, Phys. Rev. C **52**, 3470 (1995).
[16] J. Schaffner and I. N. Mishustin, Phys. Rev. C **53**, 1416 (1996).
[17] N. K. Glendenning and J. Schaffner-Bielich, Phys. Rev. C **60**, 025803 (1999). N. K. Glendenning; Phys. Rep. 342, 393 (2001).
[18] S. Pal, M. Hanauske, I. Zakout, H. Stöcker, and W. Greiner, Phys. Rev. C **60**, 015802 (1999).
[19] M. Hanauske, D. Zschiesche, S. Pal, S. Schramm, H. Stöcker, and W. Greiner, Astrophys. J. **537**, 958 (2000).
[20] P. K. Sahu, Phys. Rev. C **62**, 045801 (2000).
[21] L. Tolos, M. Centelles, and A. Ramos, Astrophys. J. **834**, 3 (2017).
[22] S. Balberg and A. Gal, Nucl. Phys. A **625**, 435 (1997).
[23] H. Huber, F. Weber, M. K. Weigel, and Ch. Schaab, Int. J. Mod. Phys. E **7**, 301 (1998).
[24] M. Baldo, G. F. Burgio, and H. -J. Schulze, Phys. Rev. C **58**, 3688 (1998); *ibid* **C 61**, 055801 (2000).
[25] I. Vidaña, A. Polls, A. Ramos, M. Hjorth-Jensen, and V. G. J. Stoks, Phys. Rev. C **61**, 025802 (2000); I. Vidaña, A. Polls, A. Ramos, L. Engvik, and M. Hjorth-Jensen; Phys. Rev. **C 62**, 035801 (2000).
[26] S. Nishizaki, Y. Yamamoto, and T. Takatsuka, Prog. Theor. Phys. **108**, 703 (2002).
[27] T. Takatsuka, Prog. Theor. Phys. Suppl. **156**, 84 (2004).
[28] H. Togashi, E. Hiyama, Y. Yamamoto, and M. Takano, Phys. Rev. **93**, 035808 (2016).
[29] M. Prakash, M. Prakash, J. M. Lattimer, and C. J. Pethick, Astrophys. J. **390**, L77 (1992).
[30] S. Tsuruta, Phys. Rep. **292**, 1 (1998).
[31] T. Muto, Phys. Rev. C **77**, 015810 (2008), and references cited therein.
[32] P. B. Demorest, T. Pennucci, S. M. Ransom, M. S. E. Roberts, and J. W. T. Hessels, Nature **467**, 1081 (2010).
[33] E. Fonseca et al. Astrophys. J **832**, 167 (2016).
[34] J. Antoniadis et al., Science **340**, 6131 (2013).
[35] H. T. Cromartie et al., Nature Astron. **4**, 72 (2020).

[36] E. Fonseca et al., arXiv:2104.00880v1 [astroph.HE] [Search inSPIRE].
[37] R. W. Romani et al., Astrophys. J. Lett. **908**, L46, (2021).
[38] S. Banik and D. Bandyopadhyay, Phys. Rev. C **63**, 035802 (2001); *ibid* **C 64**, 055805 (2001).
[39] G. Y. Shao and Y. X. Liu, Phys. Rev. C **82**, 055801 (2010).
[40] S. Pal, D. Bandyopadhyay, and W. Greiner, Nucl. Phys. A **674**, 553 (2000).
[41] A. Mishra, A. Kumar, S. Sanyal, V. Dexheimer, and S. Schramm, Eur. Phys. J. A **45**, 169 (2010).
[42] D. P. Menezes, P. K. Panda, and C. Providencia, Phys. Rev. C **72**, 035802 (2005).
[43] C. Y. Ryu, C. H. Hyun, S. W. Hong, and B. T. Kim, Phys. Rev. C **75**, 055804 (2007).
[44] P. Char and S. Banik, Phys. Rev. C **90**, 015801 (2014).
[45] V. B. Thapa and M. Sinha, Phys. Rev. D **102**, 123007 (2020).
[46] T. Malik, S. Banik, and D. Bandyopadhyay, Astrophys. J. **910**, 96 (2021).
[47] B. P. Abott et al., Phys. Rev. Lett. **119**, 161101 (2017).
[48] K. Yagi and N. Yunes, Phys. Rep. **681**, 1 (2017).
[49] B. P. Abbott et al., Phys. Rev. Lett. **121**, 161101 (2018).
[50] T. E. Riley et al., Astrophys. J. **887**, L21 (2019).
[51] M. C. Miller et al., Astrophys. J. **887**, L24 (2019).
[52] M. C. Miller et al., Astrophys. J. **918**, L28 (2021).
[53] T. E. Riley et al., Astrophys. J. Lett. **918**, L27(2021) [arXiv:2105.06980 [astro-ph HE] [Search in SPIRE]].
[54] Y. Akaishi and T. Yamazaki, Phys. Rev. C **65**, 044005 (2002); T. Yamazaki and Y. Akaishi; Phys. Lett. **B 535**, 70 (2002).
[55] T. Yamazaki, A. Dote, and Y. Akaishi, Phys. Lett. B **587**, 167 (2004).
[56] J. Yamagata, H. Nagahiro, Y. Okumura, and S. Hirenzaki, Prog. Theor. Phys. **114**, 301 (2005). J. Yamagata, H. Nagahiro, and S. Hirenzaki; Phys. Rev. **C 74**, 014604 (2006).
[57] T. Muto, T. Maruyama, and T. Tatsumi, Phys. Rev. C **79**, 035207 (2009).
[58] D. Gazda, E. Friedman, A. Gal, and J. Mares, Phys. Rev. C **76**, 055204 (2007); Phys. Rev. **C 77**, 045206 (2008); Phys. Rev. **C 80**, 035205 (2009); Nucl. Phys. **A 835**, 287 (2010).
[59] X.-R. Zhou and H.-J. Schulze, Nucl. Phys. A **914**, 332 (2013).
[60] E. Botta, T. Bressani, and G. Garbarino, Eur. Phys. J. A **48**, 41 (2012).
[61] A. Gal,E. V. Hungerford, and D. J. Millener, Rev. Mod. Phys. **88**, 035004 (2016).
[62] T. Hyodo and D. Jido, Prog. Part. Nucl. Phys. **67**, 55 (2012).
[63] Y. Ichikawa et al., Prog. Theor. Exp. Phys. **2015**, 021D01 (2015).
[64] Y. Sada et al., Prog. Theor. Exp. Phys. **2016**, 051D01 (2016).
[65] S. Ajimura et al., Phys. Lett. B **789**, 620 (2019).
[66] T. Yamaga et al., Phys. Rev. C **102**, 044002 (2020).
[67] T. Muto, T. Maruyama, and T. Tatsumi, JPS Conf. Proc. **1** 013081 (2014) EPJ Web of Conferences 73, 05007 (2014).
[68] T. Muto, T. Maruyama, and T. Tatsumi, Phys. Lett. B **820**, 136587 (2021).
[69] V. Thorsson and P. J. Ellis, Phys. Rev. D **55**, 5177 (1997).
[70] P. A. Zyla et al.[Particle Data Group], Prog. Theor. Exp. Phys. **2020**, 083C01 (2020).
[71] T. Muto, T. Maruyama, and T. Tatsumi, JPS Conf. Proc. **17**, 102003 (2017).
[72] A. D. Martin, Nucl. Phys. A **179**, 33 (1981).
[73] J. Schaffner, C. B. Dover, A. Gal, C. Greiner, D. J. Millener, and H. Stöcker, Ann. Phys. **235**, 35 (1994).
[74] D. J. Millener, C. B. Dover, and A. Gal, Phys. Rev. C **38**, 2700 (1988).
[75] M. Kohno, Y. Fujiwara, T. Fujita, C. Nakamoto, and Y. Suzuki, Nucl. Phys. A **674**, 229 (2000).
[76] Y. Fujiwara, M. Kohno, C. Nakamoto, and Y. Suzuki, Phys. Rev. C **64**, 054001 (2001).
[77] S. Bart et al., Phys. Rev. Lett. **83**, 5238 (1999).
[78] J. Dabrowski, Phys. Rev. C **60**, 025205 (1999).
[79] H. Noumi et al., Phys. Rev. Lett. **89**, 072301 (2002); Phys. Rev. Lett. 90, 049902 (2003).
[80] J. Dabrowski and J. Rożynek, Acta Phys. Polon. B **35**, 2303 (2004).
[81] T. Harada and Y. Hirabayashi, Nucl. Phys. A **759**, 143 (2005).
[82] J. Mares, E. Friedman, A. Gal, and B. K. Jennings, Nucl. Phys. A **594**, 311 (1995).
[83] T. Fukuda et al., Phys. Rev. C **58**, 1306 (1998).
[84] P. Khaustov et al., Phys. Rev. C **61**, 054603 (2000).
[85] E. Hiyama, M. Kamimura, Y. Yamamoto, and T. Motoba, Phys. Rev. Lett. **104**, 212502 (2010).

[86] G. Audi, A. H. Wapstra, and C. Thibault, Nucl. Phys. A **729**, 337 (2003).
[87] T. Gogami et al., Phys. Rev. C **93**, 034314 (2016).
[88] H. Takahashi et al., Phys. Rev. Lett. **87**, 212502 (2001).
[89] J. K. Ahn et al., Phys. Rev. C **88**, 014003 (2013).
[90] K. Nakazawa et al., Prog. Theor. Exp. Phys. **2015**, 033D02 (2015).
[91] T. T. Sun, E. Hiyama, H. Sagawa, H.-J. Schulze, and J. Meng, Phys. Rev. C **94**, 064319 (2016).
[92] S. H. Hayakawa et al., Phys. Rev. Lett. **126**, 062501 (2021).
[93] M. Yoshimoto et al., Prog. Theor. Exp. Phys. **2021**, 073D02 (2021).
[94] A. W. Steiner, J. M. Lattimer, and E. F. Brown, Astrophys. J. **722**, 33 (2010).
[95] T. Dietrich et al., Science **370**, 1450 (2020).
[96] C. Drischler, R. J. Furnstahl, J. A. Melendez, and D. R. Phillips, Phys. Rev. Lett. **125**, 202702 (2020).
[97] G. Baym and D. K. Campbell, in Mesons and Nuclei, eds M. Rho and D. H. Wilkinson, (North Holland, Amsterdam, 1979), Vol. **III**, p. 1031.
[98] S. Weinberg, Phys. Rev. Lett. **17**, 616 (1966).
[99] Y. Ichikawa et al., Prog. Theor. Exp. Phys. **2020**, 123D01 (2020).
[100] Y. Sugahara and H. Toki, Nucl. Phys. A **579**, 557 (1994).
[101] C. J. Horowitz and J. Piekarewitz, Phys. Rev. Lett. **86**, 5647 (2001).
[102] F. J Fattoyev, C. J. Horowitz, J. Piekarewicz, and B. Reed, Phys. Rev. C **102**, 065805 (2020).
[103] I. E. Lagaris and V. R. Pandharipande, Nucl. Phys. A **359**, 349 (1981).
[104] A. Akmal, V. R. Pandharipande, and D. G. Ravenhall; Phys. Rev. C **58**, 1804 (1998).
[105] T. Maruyama, T. Tatsumi, D. N. Voskresensky, and T. Tanigawa; Phys. Rev. C **73**, 035802 (2006).
[106] T. Muto, T. Maruyama, T. Tatsumi, and T. Takatsuka, JPS Conf. Proc. **20**, 011038 (2018).
[107] R. Tamagaki, Prog. Theor. Phys. **119**, 965 (2008).
[108] T. Takatsuka, S. Nishizaki, and R. Tamagaki, AIP Conf. Proc. **1011**, 209 (2008).
[109] T. Muto, T. Maruyama, and T. Tatsumi, to be submitted.
[110] S. Typel and H. H. Wolter, Nucl. Phys. A **656**, 331 (1999).
[111] Y. Yamamoto, T. Furumoto, N. Yasutake, and Th. A. Rijken, Phys. Rev. C **90**, 045805 (2014).
[112] K. Tsubakihara and A. Ohnishi, Nucl. Phys. A **914**, 438 (2013) [arXiv:1211.7208[Search inSPIRE]].
[113] T. Miyatsu, T. Katayama, and K. Saito, Phys. Lett. B **709**, 242 (2012).
[114] T. Katayama, T. Miyatsu, and K. Saito, Astrophys. J. Suppl. **203**, 22 (2012).
[115] K. Masuda, T. Hatsuda, and T. Takatsuka, Astrophys. J. **764**, 12 (2013).
[116] K. Masuda, T. Hatsuda, and T. Takatsuka, Prog. Theor. Exp. Phys. **2016**, 021D01 (2016).
[117] T. Kojo, P. D. Powel, Y. Song, and G. Baym, Phys. Rev. D **91**, 045003 (2015).
[118] P. F. Bedaque and T. Schäfer, Nucl. Phys. A **697**, 802 (2002).
[119] D. B. Kaplan and S. Reddy, Phys. Rev. D **65**, 054042 (2002).
[120] M. Buballa, Phys. Lett. B **609**, 57 (2005).
[121] M. M. Forbes, Phys. Rev. D **72**, 094032 (2005).
[122] S. Banik and D. Bandyopadhyay, Phys. Rev. D **67**, 123003 (2003).
[123] J. Gasser, H. Leutwyler, and M. E. Sainio, Phys. Lett. B **253**, 252 (1991).
[124] H. Ohki[JLQCD Collaboration] et al. [JLQCD Collaboration], Phys. Rev. D **78**, 054502 (2008).
[125] R. D. Young and A. W. Thomas, Nucl. Phys. A **844**, 266c (2010); Phys. Rev. **D 81**, 014503 (2010).
[126] Y. B. Yang, A. Alexandru, T. Draper, J. Liang, and K.-F. Liu [χQCD Collaboration], Phys. Rev. D **94**, 054503 (2016).